

# Whole-Body Imaging with Single-Cell Resolution by Tissue Decolorization

Kazuki Tainaka,<sup>1,2,3,4</sup> Shimpei I. Kubota,<sup>1,4</sup> Takeru Q. Suyama,<sup>1</sup> Etsuo A. Susaki,<sup>1,2,3</sup> Dimitri Perrin,<sup>2</sup> Maki Ukai-Tadenuma,<sup>2</sup> Hideki Ukai,<sup>2</sup> and Hiroki R. Ueda<sup>1,2,3,\*</sup>

<sup>1</sup>Department of Systems Pharmacology, Graduate School of Medicine, The University of Tokyo, 7-3-1 Hongo, Bunkyo-ku, Tokyo 113-0033, Japan

<sup>2</sup>Laboratory for Synthetic Biology, RIKEN Quantitative Biology Center, 2-2-3 Minatojima-minamimachi, Chuo-ku, Kobe, Hyogo 650-0047, Japan

<sup>3</sup>CREST, Japan Science and Technology Agency, 4-1-8 Honcho, Kawaguchi, Saitama 332-0012, Japan

<sup>4</sup>Co-first author

\*Correspondence: [uedah-ky@umin.ac.jp](mailto:uedah-ky@umin.ac.jp)  
<http://dx.doi.org/10.1016/j.cell.2014.10.034>

## SUMMARY

The development of whole-body imaging at single-cell resolution enables system-level approaches to studying cellular circuits in organisms. Previous clearing methods focused on homogenizing mismatched refractive indices of individual tissues, enabling reductions in opacity but falling short of achieving transparency. Here, we show that an aminoalcohol decolorizes blood by efficiently eluting the heme chromophore from hemoglobin. Direct transcardial perfusion of an aminoalcohol-containing cocktail that we previously termed CUBIC coupled with a 10 day to 2 week clearing protocol decolorized and rendered nearly transparent almost all organs of adult mice as well as the entire body of infant and adult mice. This CUBIC-perfusion protocol enables rapid whole-body and whole-organ imaging at single-cell resolution by using light-sheet fluorescent microscopy. The CUBIC protocol is also applicable to 3D pathology, anatomy, and immunohistochemistry of various organs. These results suggest that whole-body imaging of colorless tissues at high resolution will contribute to organism-level systems biology.

## INTRODUCTION

Since the discovery of cells in the organism about 350 years ago, whole-body imaging of single cells in opaque organisms like mammals has been a fundamental challenge in biology and medicine. Imaging intact structures at single-cell resolution will enable a systems-level elucidation of cellular connectivity and dynamics. This will improve our understanding of the generation and progression of diseases with stochastic and proliferative processes such as autoimmune and malignant neoplastic diseases, because single-cell events in these diseases eventually

affect the health status of the entire organism. However, even the ~30 g body of an adult mouse comprises more than 30 billion cells, which makes it difficult to comprehensively identify cellular circuits and quantitatively analyze dynamics. Conventional histology techniques are laborious and require tissue sectioning, which are challenging barriers toward rapid three-dimensional (3D) visualization of organ structures.

By contrast, optical sectioning with light-sheet microscopy in combination with recent advances in tissue-clearing techniques is a promising route toward visualizing single cells within a whole-organ or whole-body context (Dodt et al., 2007; Ertürk et al., 2012; Keller and Dodt, 2012; Susaki et al., 2014; Tomer et al., 2014). The pioneering work by Werner Spalteholz first introduced the principle of transparent 3D specimens a century ago (Spalteholz, 1914). Up until now, a number of tissue-clearing reagents (BABB, THF-DBE, Scale, SeeDB, Clear<sup>T</sup>) and protocols (3DISCO, CLARITY, PACT-PARS) have been developed (Becker et al., 2012; Chung et al., 2013; Dodt et al., 2007; Ertürk et al., 2012; Hama et al., 2011; Ke et al., 2013; Kuwajima et al., 2013; Tomer et al., 2011; Yang et al., 2014). However, they cleared tissues to different degrees of transparency. In order to observe deep tissue structures, we aimed for a level of transparency of internal organs (such as heart, lung, kidney, liver, pancreas, spleen, stomach, and small and large intestines) and soft tissues (such as muscles) to the extent that: (1) chest and abdominal backbones and the bones of limbs through internal organs and soft tissues from both ventral and dorsal sides of the body are visible, and (2) individual cells within intact organs and tissues are resolved by whole-body or whole-organ imaging. We previously demonstrated that aminoalcohol-based chemical cocktails, termed CUBIC (clear, unobstructed brain imaging cocktails and computational analysis), efficiently cleared whole brains of adult mice by removing lipids to homogenizing refractive indices (RIs) without signal loss from fluorescence proteins (Susaki et al., 2014). All previous tissue-clearing methods, including ours, have mainly focused on homogenizing RIs, and some of them based on the lipid removal (BABB, 3DISCO, CLARITY, CUBIC, PACT-PARS) succeeded in the clearing and imaging of adult whole brain (Becker et al., 2012; Chung et al., 2013; Dodt et al.,

2007; Ertürk et al., 2012; Susaki et al., 2014; Yang et al., 2014), which is a relatively lipid-rich tissue. However, when applied to the whole body, thick tissues block photons in the visible region (400–600 nm) not only because of light scattering by endogenous materials with mismatched RIs, but also because of the light absorbance by endogenous chromophores—mainly hemoglobin and myoglobin (Faber et al., 2003; Weissleder, 2001). Thus, efficient decolorization of endogenous chromophores inside tissues (particularly heme, which is one of the most abundant endogenous chromophores) is needed to clear whole-body tissues. Classical treatment by the peroxide decolorizes tissues. However, this peroxide treatment causes not only serious damage to outer tissues (Steinke and Wolff, 2001), but also a significant loss of GFP signal (Alnuami et al., 2008). Heme tightly binds to hemoglobin and can be released only in highly acidic ( $\leq$ pH 2) or basic ( $\geq$ pH 11) conditions (Kristinsson and Hultin, 2004; Teale, 1959). This highly acidic or basic treatment also results in significant loss of signals from GFP-related fluorescence proteins (Haupts et al., 1998). Thus, a clearing method is needed to efficiently elute heme in moderately basic conditions to enable GFP-related fluorescence proteins to retain their fluorescence properties.

In this study, we demonstrate that aminoalcohols within CUBIC cocktails decolorized the blood by efficiently eluting the heme chromophore from hemoglobin in moderately basic conditions. An accelerated clearing protocol with CUBIC perfusion rendered nearly transparent almost all organs of adult mice, as well as the entire bodies of infant and adult mice, and enabled rapid whole-body and whole-organ imaging with single-cell resolution. We used CUBIC to diagnose the pathology of Langerhans islets in the diabetic pancreas, as well as to anatomically annotate various organ structures in 3D. We also applied CUBIC to 3D immunohistochemistry of various organs. These results suggest that whole-body imaging with single-cell resolution achieved by tissue decolorization can contribute to the foundation of the organism-level systems biology.

## RESULTS

### Aminoalcohols in CUBIC Cocktails Decolorized the Blood by Efficiently Eluting Heme Chromophore

To achieve whole-body imaging with single-cell resolution, it is important to decolorize endogenous chromophores such as heme. When we immersed various organs directly (i.e., without perfusion) to paraformaldehyde (PFA) and subjected them to Sca/eCUBIC-1 (Susaki et al., 2014; in this study, we term it “CUBIC-1” for simplicity), we found that the color of the solvent immediately turned a dark green. This observation led us to hypothesize that CUBIC-1 could solubilize and elute endogenous heme from blood-infused tissues. To test this hypothesis, we first investigated whether CUBIC reagents can directly decolorize blood. The PFA-fixed blood suspension was washed three times with CUBIC-1, resulting in transparent pellet and olive-green supernatant (Figure 1A). On the other hand, the pellet and the supernatant from PBS-treated blood suspension remained dark red and colorless, respectively. Among CUBIC-1 constituents, *N,N,N',N'*-tetrakis(2-hydroxypropyl)ethylenediamine (termed here as “aminoalcohol #10”) (Susaki et al.,

2014) alone, but not other reagents, is sufficient to decolorize the blood (Figures 1A and 1B). The visible spectra of chemically treated erythrocytes were recorded to investigate what kind of olive-green molecule was eluted from the blood into the supernatant. The visible spectrum from the PBS-treated erythrocyte suspension is quite different from that of erythrocyte suspension treated by 0.1 M NaOH (initial pH = 13), aminoalcohol #10 and CUBIC-1 reagent (Figure 1C). We also recorded the visible spectra from purified heme (free heme chromophore released from hemoglobin), purified biliverdin (which is a product of heme catabolism), iron(II) chloride, erythrocytes, and supernatant of PFA-fixed blood treated by aminoalcohol #10 (Figure 1D) or CUBIC-1 reagent (Figure S1A available online). The normalized spectra of the erythrocyte and supernatant overlapped almost completely with hemin solutions in aminoalcohol #10 or CUBIC-1, which suggests that heme is released from hemoglobin in erythrocytes when treated by aminoalcohol #10 or the CUBIC-1 reagent.

We noted that aminoalcohol #10 and CUBIC-1 reagent have buffering capacity in pH 9–11 whereas other reagents did not (Figure S1B). If buffering capacity in basic pH is critical for the decolorizing capability, we predicted that a basic solution containing 0.01 M NaOH, which usually elutes heme from hemoglobin, will lose its decolorizing capability at a higher concentration of erythrocytes because the higher concentration of cells will shift the pH from basic to neutral. To test this prediction, we prepared a mixture of erythrocytes and these chemicals at different ratios (Figure 1E). Although urea and Triton X-100 in basic solution moderately promoted heme release at high chemical ratios, these were less effective at lower concentrations. On the other hand, aminoalcohol #10 and CUBIC-1 reagent promoted heme release even at high erythrocyte ratios. As shown in Figure 1C, the absorbance ratio between 600 nm and 575 nm can be used as a quantitative index for the efficiency of heme release. OD600/OD575 values of samples from Figure 1E were therefore plotted against erythrocyte/chemical ratio (Figure S1C). These results quantitatively confirmed that aminoalcohol #10 in the CUBIC-1 reagent can efficiently promote heme release regardless of the erythrocyte/chemical ratio and can work as a decolorizing buffer at moderate basic pH. We evaluated the pH dependence on the efficiency of heme release for aminoalcohol #10, CUBIC-1 reagent, and non-buffered basic solution, respectively (Figure 1F). In non-buffered basic solution, heme was efficiently released from hemoglobin, but only at pH >11, as previously reported (Kristinsson and Hultin, 2004). On the other hand, aminoalcohol #10 efficiently eluted heme even in moderately basic conditions around pH 10, which is within the optimal pH range for fluorescence signal intensity of GFP-related fluorescence proteins (Haupts et al., 1998). CUBIC-1 reagent further promoted heme release even around pH 9, which might be attributed to a combinatorial effect with urea and/or Triton X-100. These results suggested that aminoalcohol #10 in CUBIC-1 reagent expanded the pH window for efficient heme release. To clarify the chemical properties of aminoalcohol #10 associated with its decolorizing capability, we investigated erythrocyte with a series of aminoalcohol derivatives (Figures S1D and S1E). These results revealed the chemical properties (i.e., higher amines without carboxylic groups)

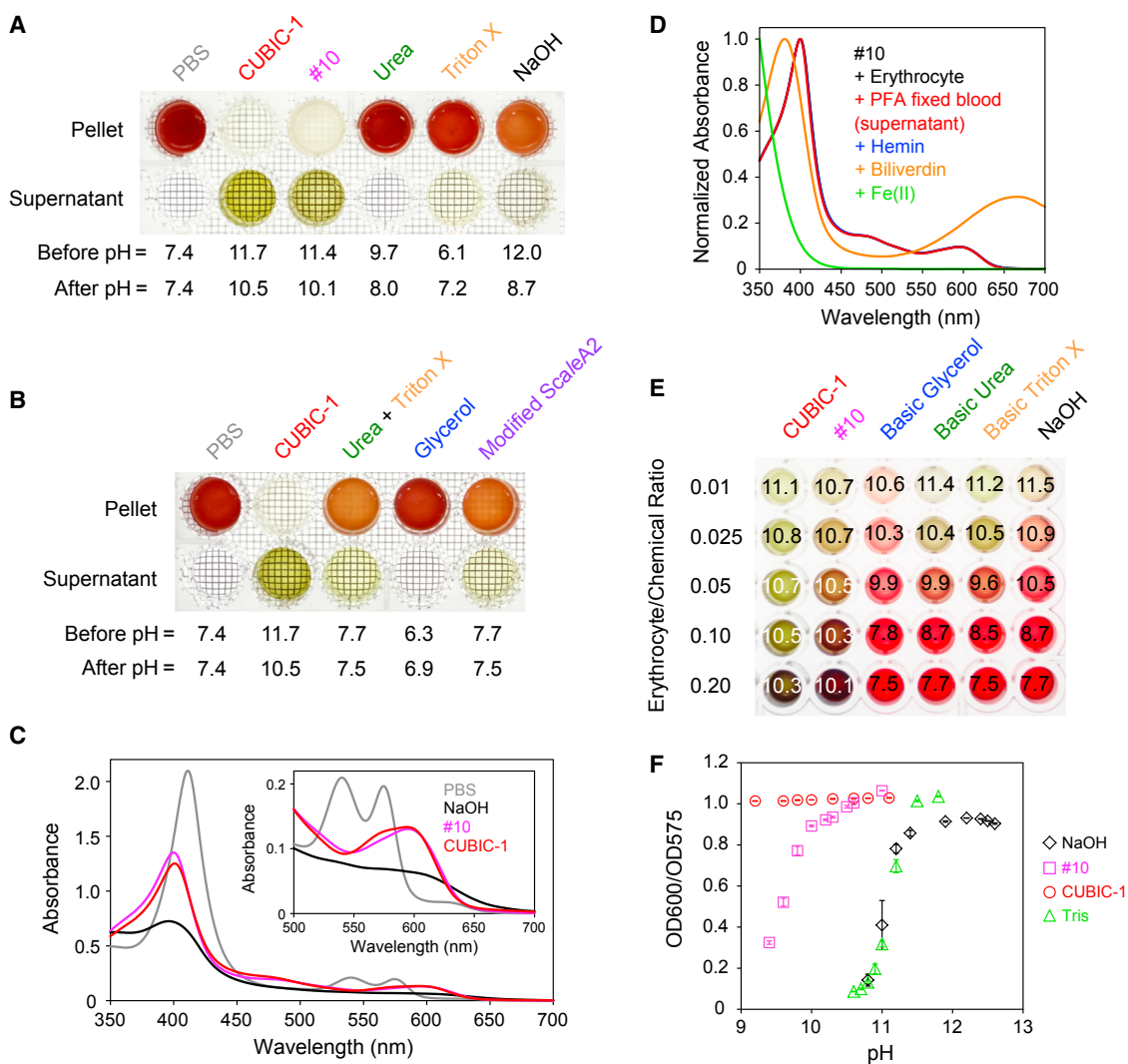


**Figure 1. Aminoalcohols in CUBIC Cocktails Decolorized the Blood by Efficiently Eluting Heme Chromophore**

(A) Decolorizing of the PFA-fixed blood by the previously published CUBIC-1 cocktail (“CUBIC-1”) and its constituents. Numbering of aminoalcohol #10 was derived from the previous chemical screening. Bright-field images of pellet and supernatant from fixed blood samples washed with PBS, CUBIC-1 reagent, 25 wt% aminoalcohol #10, 25 wt% urea, 15 wt% Triton X-100, or 0.01 M NaOH, respectively. pH of the original liquid and supernatant is shown at the bottom.

(B) Decolorizing PFA-fixed blood by CUBIC-related chemicals. Bright-field images of pellet and supernatant from PFA-fixed blood samples washed with PBS, CUBIC-1 reagent (“CUBIC-1”), a mixture of 25 wt% urea and 15 wt% Triton X-100 (“Urea + Triton X”), 25 wt% glycerol (“Glycerol”), or a mixture of 25 wt% urea, 25 wt% glycerol and 15 wt% Triton X-100 (“Modified ScaleA2”), respectively. pH of the original liquid and supernatant is shown at the bottom.

(C) Visible spectra of a chemically treated 0.1% mouse erythrocyte suspension. Erythrocytes were mixed with PBS (gray), 0.1 M NaOH (black), aminoalcohol #10 (magenta), or CUBIC-1 reagent (red), and were incubated at 37°C overnight. Inset: magnification of the Q-band region.

(D) Normalized spectra of 0.1% mouse erythrocyte (black), 1/10 diluted supernatant from (A) (red), 10  $\mu$ M hemin (blue), 10  $\mu$ M biliverdin (orange), and 100  $\mu$ M iron(II) chloride (green), in 25 wt% aminoalcohol #10.

(E) Aminoalcohol #10 in CUBIC reagents facilitates the release of heme independent of the mixing ratio with erythrocytes. Bright-field images of the 1% to 20% erythrocyte suspension mixed with CUBIC-1 reagent, 25 wt% aminoalcohol #10, 25 wt% basic glycerol, 25 wt% basic urea, 15 wt% basic Triton X-100, and 0.01 M NaOH. Indicated value in each well corresponds to pH.

(F) Aminoalcohol #10 in CUBIC reagents significantly expands the pH range of heme release. 1% erythrocyte suspension including 1–100 mM NaOH (black diamond,  $n = 3$ ), aminoalcohol #10 (pH = 9.4–11.0, magenta square,  $n = 3$ ), CUBIC-1 (pH = 9.2–11.1, red circle,  $n = 3$ ), and 25 wt% tris(hydroxymethyl)amino-methane (pH = 10.6–11.8, green triangle,  $n = 3$ ) incubated at 37°C overnight. Visible spectra of these samples were recorded. Because OD600/575 correlates with the efficiency of heme release, OD600/575 of these samples is plotted against pH. Data represent the average  $\pm$  SD. See also Figure S1.

associated with efficient decolorizing and might reflect the affinity of these chemicals to the heme chromophore. Overall, aminoalcohol in CUBIC reagents critically contributed to blood

decolorization, which is assisted by its chemical capacities to buffer pH in moderately basic conditions and to expand the pH window for efficient heme release.

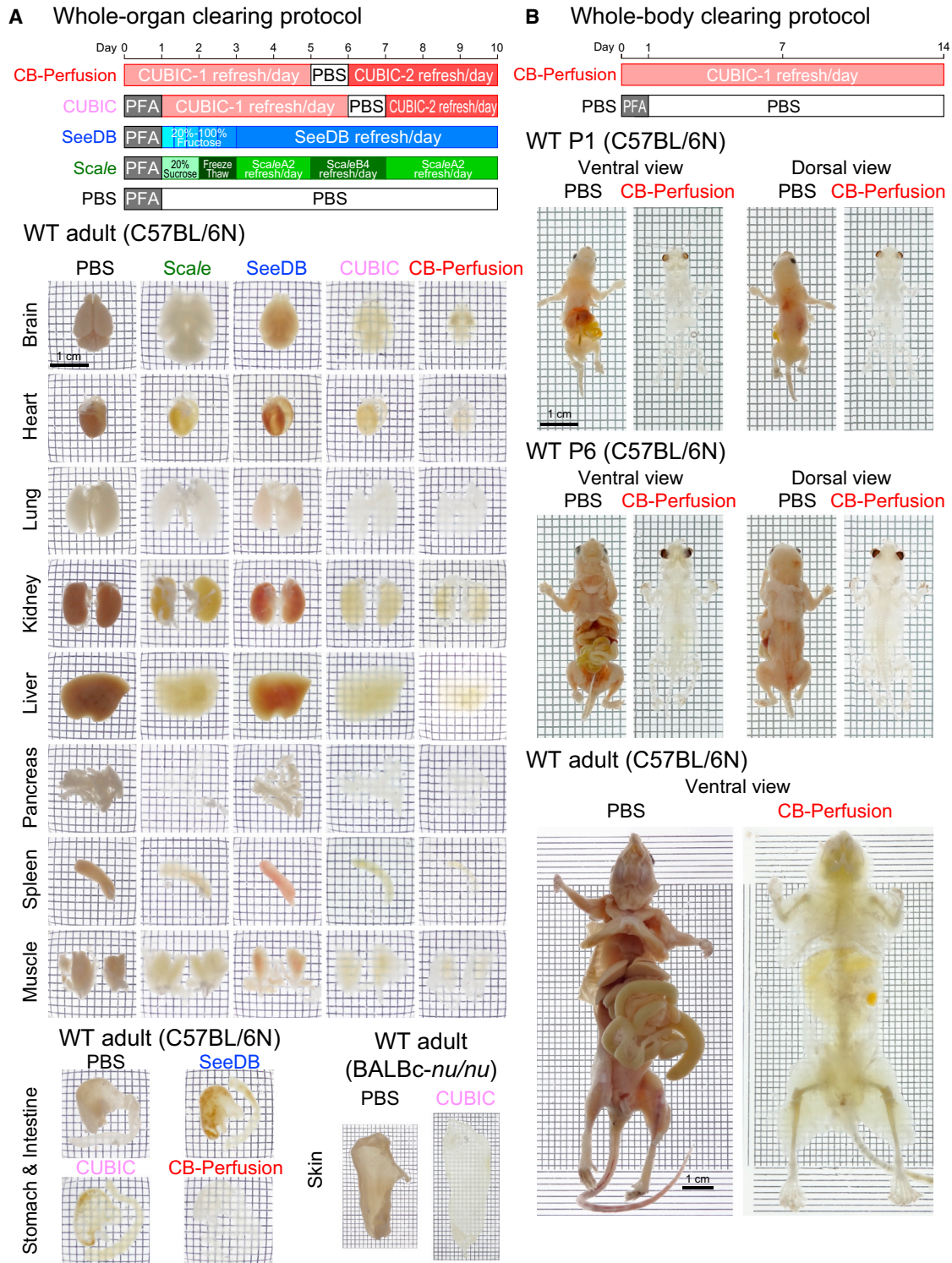


**Figure 2. CUBIC Provides a Simple and Efficient Whole-Organ and Whole-Body Clearing Protocol**

(A) (Top) Whole-organ clearing protocol in 10 days. (Middle) Transmission images of whole organs (brain, heart, lung, kidney, liver, pancreas, spleen, and muscle) from adult C57BL/6N. In the CB-Perfusion protocol, deeply anesthetized mice were sacrificed and transcardially perfused with PBS, 4% PFA/PBS (w/v), and 1/2 diluted CUBIC-1 reagent. The excised organs were further cleared by CUBIC-1 reagent without postfixation in 4% PFA/PBS. (Lower-left) Bright-field images of whole stomach and intestine from C57BL/6N treated with the CUBIC, CB-Perfusion protocol, SeeDB, or PBS using 10-day clearing protocol (Scale-treated

(legend continued on next page)

### CUBIC Is a Simple and Efficient Whole-Organ and Whole-Body Clearing Protocol

In this study, we focused on the development of an immersion-only tissue-clearing protocol based on hydrophilic clearing reagents (Extended Experimental Procedures). We evaluated the clearing performance of Scale, SeeDB, and CUBIC protocols in various organs (Hama et al., 2011; Ke et al., 2013; Susaki et al., 2014). Each protocol was based on the experimental conditions of the original papers, as shown in Figure 2A, except for a daily exchange of the clearing medium. We measured the temporal development of average transmittance of different organs (brain, heart, lung, kidney, and liver) with each protocol (Figure S2A) and obtained transmittance curves of these organs around the visible region after 10 days (Figure S2B). The CUBIC protocol was superior to other methods in both clearing kinetics and plateau performance in transmittance for all organs studied. We confirmed that the CUBIC protocol enhanced the transmittance of organs in the 480–680 nm range, as expected from the decolorizing capability of CUBIC reagents. Bright-field images of different organs (brain, heart, lung, kidney, liver, pancreas, spleen, muscle, stomach and intestine, and skin) after 10 days also demonstrated that all organs treated with CUBIC reagents resulted in the most transparent and decolorized images (Figure 2A).

Based on the blood decolorizing capability of the CUBIC-1 reagent, transcatheter perfusion of this reagent (and hence the blood decolorization through blood vessels) will enhance whole-organ and whole-body clearing. We thus developed a CUBIC perfusion (CB-Perfusion) protocol to achieve whole-organ and whole-body clearing. In the original CUBIC protocol, tissues were conventionally fixed by transcatheter perfusion of 4% PFA (25–50 ml) and were immersed in 4% PFA at 4°C overnight as a postfixation. In the advanced CB-Perfusion protocol, tissues in the entire body were fixed by prolonged transcatheter perfusion of 4% PFA (150 ml) and were then cleared by subsequent transcatheter perfusion of 1/2 diluted CUBIC-1 reagents (20 ml). Each organ was then extracted and further cleared by CUBIC reagents. The CB-Perfusion protocol accelerated the clearing kinetics and further enhanced the plateau performance in transmittance when compared with the original CUBIC protocol (Figures S2A and S2B). In a bright-field imaging comparison of all organs, the CB-perfused organs were the clearest (Figure 2A). These results indicate successful development of the whole-organ clearing protocol, which finishes within 10 days.

We next attempted whole-body clearing of infant (postnatal day 1 [P1] and P6) and adult mice (19-week-old) by using this CB-Perfusion protocol. After transcatheter perfusion of 4% PFA and 1/2 diluted CUBIC-1 reagent and subsequent detachment of skin, the entire body was cleared by the CUBIC-1 reagent. We noticed that the clearing medium (CUBIC-1 reagent) immediately turned a dark green color probably due to decolorization of endogenous chromophores (mainly heme). To facilitate the whole-body clearing, clearing medium were refreshed daily for

2 weeks. The clearing medium gradually became less colored, and after 2 weeks, the apparent transparency of the whole body became saturated. Whole-body samples can be then stored in CUBIC-1 reagent and even shaken at 37°C over months because the high pH of CUBIC-1 reagents prevents proliferation of microorganisms. Bright-field images of infant mice (P1 and P6) demonstrated that CB-Perfusion protocol transparentized and decolorized P1 and P6 infant mice (Figure 2B). We confirmed the visualization of chest and abdominal backbones as well as bones of limbs through internal organs and soft tissues from both ventral and dorsal sides of the body. Bright-field images of adult mice (19-week-old) demonstrated that CB-Perfusion protocol also markedly transparentized and decolorized adult mice (Figures 2B and S2C). The bones of forelimbs (including scapula, humerus, radius, and ulna) and hindlimbs (including femur, tibia, and fibula) and caudal vertebrae were clearly visualized in either V-D or the dorsal-to-ventral (D-V) images of adult mice.

### CUBIC Is Applicable to Whole-Body Imaging of Infant and Adult Mice with Single-Cell Resolution

The high transparency of CB-perfused samples prompted us to perform light-sheet fluorescence microscopy (LSFM). As previously described, the CUBIC protocol is compatible with whole-brain nuclear counterstaining (Susaki et al., 2014). We thus applied nuclear counterstaining by propidium iodide (PI) to whole-body samples and imaged PI-stained CAG-EGFP transgenic (Tg) (Okabe et al., 1997) P1 mouse transparentized and decolorized by the CB-Perfusion protocol. Whole-body images were obtained from two opposite directions (D-V and V-D) (Figure 3A). Both images were sufficiently clear even at 4–5 mm depth. Nuclear staining with PI tends to highlight non-muscular organs and solid tissues, whereas CAG-EGFP signals were more intense in the muscular organs such as heart and subcutaneous tissue. Magnified images from the same sample were also obtained to visualize internal structures of head, chest, abdominal, and pelvic organs as well as limbs (Figures 3B, S3A, and S4). These images were then deconvolved by AutoQuant X3 software (we denoted the deconvolved images as prefix “DCV-” in the figures). For example, the granule duct in the submaxillary gland, coronary vessels in the heart, bronchiole in the lung, gastric walls in the stomach, vascular structures in the liver, renal cortex and medulla in the kidney, villus in the intestine, and penis and testis in the scrotum were clearly identified in each z stack image (Figure S4). Surprisingly, detailed structures in hippocampus and cerebellum were visible through the skull, central canal inside the spinal cords were seen through vertebrae, and internal structures of tibia in the leg were also visualized (Figures 3B and S4). We note that the magnified images of these organs resolved to single-cell levels (Figure 3C, top). We also performed whole-body imaging of PI-stained CAG-EGFP Tg P6 mouse transparentized and decolorized by the

stomach and intestine were usually fragile and torn during the procedure due to proliferation of microorganisms; thus it was impossible to take comparison data). (Lower-right) Bright-field images of skin from BALB/c-*nu/nu* treated with CUBIC reagents and PBS using the 10-day clearing protocol.

(B) Whole-body clearing protocol in 2 weeks. Bright-field images (ventral and dorsal view) of whole body (C57BL/6N P1, P6, and adult mice) stocked in PBS after fixation or subjected to the CB-Perfusion protocol. 8-week-old mouse for the PBS sample and 19-week-old mouse for the cleared sample are shown.

See also Figure S2.

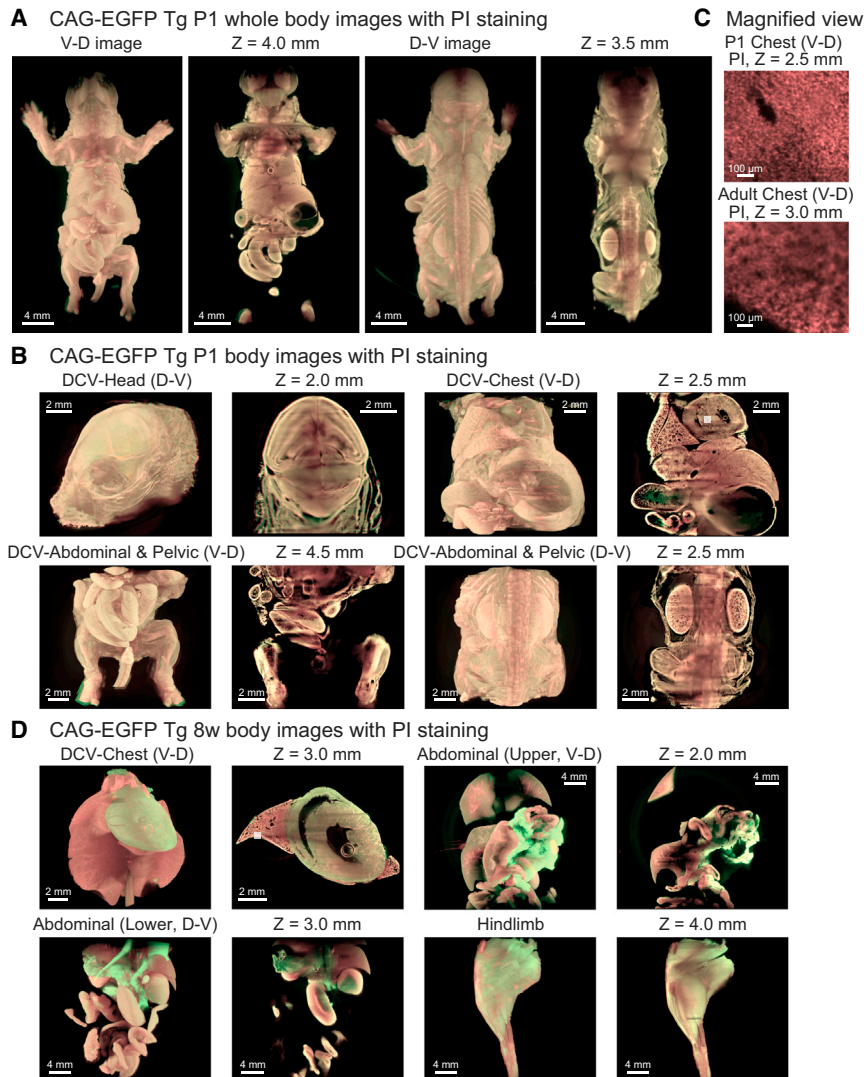


### Figure 3. CUBIC Is Applicable to Whole-Body Imaging of Infant and Adult Mice with Single-Cell Resolution

(A) 3D-reconstituted and X-Y plane (indicated with Z position), lower-resolution whole-body images of PI-stained CAG-EGFP Tg P1 mouse. Images were acquired with light-sheet fluorescence microscopy (LSFM) from the ventral-to-dorsal (V-D) and dorsal-to-ventral (D-V) directions, respectively.

(B) 3D-reconstituted and X-Y plane body images of PI-stained CAG-EGFP Tg P1 mouse. Head (D-V), chest organs (V-D), abdominal, and pelvic organs (V-D and D-V) are shown. All images were deconvolved with AutoQuant X3 software. Prefix “DCV-” indicates the deconvolved image.

(C) Magnified images in (B) (Chest, Z = 2500) and (D) (Chest, Z = 3000) indicating these images taken with single-cell resolution. Each dot is PI signals of single cell nucleus.

(D) 3D-reconstituted and X-Y plane body images of the PI-stained CAG-EGFP Tg adult mouse (8-week-old). Chest organs (V-D), upper abdominal organs (V-D), lower abdominal organs (D-V), and hindlimb are shown. Enlarged parts in (C) are indicated as a white box in (B) and (D). Prefix “DCV-” indicates the deconvolved image.

See also Figures S3 and S4.

CB-Perfusion protocol. Because the P6 mouse was too large to be captured in a single view, we obtained whole-body images from three views (head, chest, and abdomen, Figure S3C). The quality of whole-body images of P6 mice was almost comparable to that of P1 mice and visualized the internal structures of head, chest, abdominal, and pelvic organs as well as limbs.

We next performed whole-body imaging of PI-stained CAG-EGFP Tg adult mice (8-week-old) transparentized and decolorized by the CB-Perfusion protocol. Adult mice bodies could not fit into existing LSFMs, so we dissected the adult body into four parts (chest organs, abdominal organs, forelimbs, and hindlimbs) and then obtained their images (Figures 3D and S3B). Adult mouse tissues exhibited much higher contrast between PI and EGFP signals than those of infant mice. For example, EGFP signals were much higher in heart, pancreas, stomach, and muscles probably because EGFP expression from CAG promoter in these organs was elevated. In z stack images of chest organs, ventricle structures in the heart and bronchiole in the lung can be clearly visualized (Figure 3D). In z stack images of

internal structures of entire body regions (chest and abdominal organs, forelimb, and hindlimb) with single-cell resolution.

### CUBIC Is Applicable to Whole-Organ Imaging with Single-Cell Resolution

For rapid whole-organ imaging, we used a knockin (KI) mouse strain expressing three tandem repeats of *mKate2* with a nuclear localization signal, under control of the CAG promoter (Niwa et al., 1991) from the 3'-UTR of  $\beta$ -actin gene locus (Tanaka et al., 2012). We used *mKate2* because of its signal intensity, photostability, and rapid protein maturation (Chudakov et al., 2010; Shcherbo et al., 2009), as well as its resistance to fluorescence quenching by CUBIC reagents, as previously described (Susaki et al., 2014). We then performed whole-organ imaging of various CB-perfused organs, including heart, lung, kidney, liver, pancreas, spleen, muscle, stomach, and intestine from this  $\beta$ -actin-nuc-3 x *mKate2* KI mouse (8-week-old) and counterstained with SYTO 16, a cell-permeable green-fluorescent nucleic acid stain. The resulting 3D-reconstituted image of each organ in this *mKate2* KI

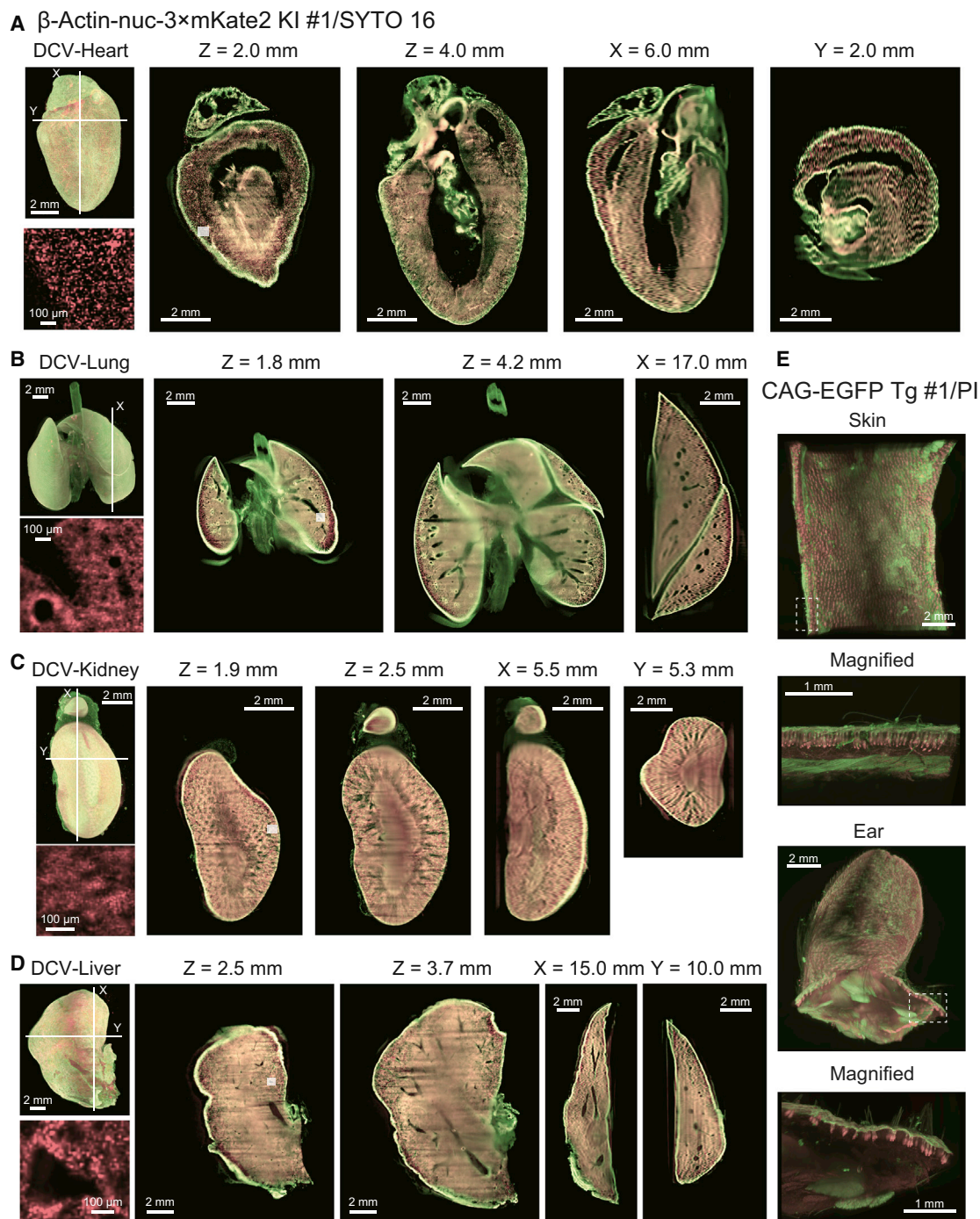


**Figure 4. CUBIC Is Applicable to Whole-Organ Imaging with Single-Cell Resolution**

The reconstituted 3D and section images of a heart (A), lung (B), kidney (C), and liver (D) from nuclear-stained  $\beta$ -actin-nuc-3  $\times$  mKate2 KI mouse (8-week-old) and skin and ear (E) from CAG-EGFP Tg mouse (10-week-old) were acquired with LSM. Raw X-Y section images and reconstituted Y-Z and X-Z section images are at the indicated positions. Prefix “DCV-” indicates the deconvolved image. In (A–D), enlarged images indicated by a white box on z plane images are shown, indicating that these images are taken at single-cell resolution. Each dot is nuclear-localized mKate2 signals from single cell nuclei. See also Figures S5 and S6.

mouse, as well as its horizontal, coronal, and sagittal sections, enabled the visualization of spatial gene expression patterns (from the CAG promoter at  $\beta$ -actin 3'-UTR) and examination of

detailed internal structures (Figures 4A–4D and S5A–S5F). For example, 3D reconstitution images of the heart successfully visualized not only lumens of atria and ventricle, but also internal

papillary muscle, coronary vascular structures, and even valve structures (Figure 4A). In lungs, the networks of trachea, bronchi, and bronchiole in both lobes were clearly identified (Figure 4B). In the kidney, 3D reconstitution images easily distinguished between renal cortex, medulla, and pelvis (Figure 4C). In the liver, two kinds of vascular structures were identified as thicker vessels, which would indicate the hepatic artery, and thinner vessels, which would indicate the portal vein (Figure 4D). Langerhans islets and pancreatic ducts were identified in the pancreas (Figure S5A). Splenic white pulp and red pulp were identified in the spleen (Figure S5B). Orientations of muscle fibers and blood vessels were observed in the muscle (Figure S5C). Corpus glands were significantly highlighted, and pylorus and cardia were clearly observed in the stomach (Figure S5D). Mesentery and villi were seen in the intestine (Figure S5E). We also obtained 3D reconstitution images of brain as well as kidney and muscle, which are contralateral to those in Figures 4C and S5C from the identical mouse body (Figure S5F). In addition to imaging internal organs and muscles, we collected skin and ears from pelage-removed CAG-EGFP Tg mouse and subjected them to CUBIC reagents with nuclear-counterstain PI. We then performed whole-organ imaging of these tissues (Figure 4E). EGFP signals highlighted epidermis, muscle layer under hypodermis, and residual pelage, whereas PI signal intensity was relatively higher in hair matrix cells. Taken together, these results demonstrate that CUBIC enables whole-organ imaging with single-cell resolution of almost all organs by using various fluorescence proteins.

The successful whole-organ imaging using mKate2 led us to test other fluorescence proteins, including EGFP and YFP. We performed similar whole-organ imaging of each organ from three strains of CB-perfused adult mice: CAG-EGFP Tg (Figure S6A), an EGFP-fused histone-2B-expressing strain (R26-H2B-EGFP [CDB0239K]; Figure S6B) (Abe et al., 2011), and a Thy1-YFP-H Tg strain (Figure S6C) (Feng et al., 2000), respectively. PI was used as nuclear staining for whole-organ imaging of these strains. When we captured the section images of each organ from CAG-EGFP Tg (Figure S6A) and  $\beta$ -actin-nuc-3  $\times$  mKate2 KI mice (Figures 4 and S5), the spatial distribution of fluorescence proteins (EGFP and nuc-3  $\times$  mKate2) was markedly different. This is because EGFP was localized in the nucleus and cytosol, whereas mKate2 was localized only in the nucleus. Similarly, we could obtain 3D reconstitution images of whole organs from R26-H2B-EGFP and the neuronal marker Thy1-YFP-H (Figures S6B and S6C). These results demonstrate that CUBIC protocol enables whole-organ imaging with various fluorescence proteins (mKate2, EGFP, and YFP) and that whole-organ imaging with single-cell resolution can extract 3D single-cell information of internal anatomical structures in different organs.

### CUBIC Is Applicable to 3D Pathology of Langerhans Islets in the Diabetic Pancreas

One attractive application of whole-body and whole-organ imaging with single-cell resolution is 3D pathology of organs. To test this potential, we investigated the spatial distribution of Langerhans islets (LIs) in diabetic and normal pancreases by using the CB-Perfusion protocol. As a model, we first focused on diabetic pancreases because BABB-based analysis combined with optical projection tomography (OPT) has already been applied

(Alanentalo et al., 2007). Streptozotocin (STZ) is a well-known cytotoxic agent for pancreatic  $\beta$  cells, which disrupts the ability of  $\beta$  cells to secrete insulin and stabilize blood sugar levels (King, 2012). High-dose STZ injection destroys  $\beta$  cells, which are major constituents of LIs and induce type I diabetes mellitus. LIs contract because of  $\beta$  cell destruction after the onset of diabetes. We therefore performed comprehensive and statistical analysis of diabetic LIs in the whole pancreas of adult mice. We dissected and transparentized pancreases from saline-treated control mice ( $n = 3$ ) and acute type I diabetic mice ( $n = 3$ , whose blood sugar levels were over 400 mg/dl as shown in Table S1) by the CB-Perfusion protocol with PI staining. Acquired images enabled us to morphologically distinguish the characteristic clusters (LIs) from the characteristic tracts (pancreatic ducts) (Figure 5A). We identified and 3D reconstituted all LIs according to Figure 5A and Extended Experimental Procedures. The image analysis also provided a spatial distribution of LIs in the pancreas. For example, larger LIs tend to be localized along pancreatic ducts. By using the extracted LI data, we can compare the total number of LIs between diabetic and healthy mice. As expected, the average number of LIs was significantly reduced by the onset of diabetes (Figure 5B, left,  $p = 0.005$ ). The differences of average LI volume between diabetic and healthy mice were also marginally significant (Figure 5B, center,  $p = 0.09$ ), which is consistent with the observed reduction in the existence probability of larger LIs in diabetic mice ( $>1.0 \times 10^7 \mu\text{m}^3$ , Figure 5B, right). These data indicate that larger LIs are more susceptible to  $\beta$  cell impairment induced by STZ administration. Overall, these results indicate that CUBIC enables 3D pathology of a diabetic pancreas.

### CUBIC Is Applicable to 3D Anatomy of Various Organs

The successful 3D pathology of diabetic pancreases prompted us to generalize this to 3D anatomy of various organs, which may provide a versatile platform for elucidation of cellular mechanisms underlying the physiology and pathology of observed anatomical structures. As a test case, we analyzed whole-heart images from mKate2 KI mouse. We noted that mKate2 signals are more intense in the surface of the tracts, which can be morphologically annotated as coronary vessels (Figure 6A). We extracted, by using the surface analysis in the Imaris software, high-intensity signals in the heart and excluded the surfaces of smaller volume size, resulting in 3D images of coronary vessels covering the entire heart (Figure 6A and Movie S1). Internal structures such as tendinous cords and valves could be also visualized (Figure S7A). We also analyzed whole-lung images from the same mKate2 KI mouse. We noted that mKate2 signals in respiratory tract fall to undetectable levels, and thus we can extract low-intensity signals in the lungs, resulting in a bronchial tree covering the entire lung (Figure 6B and Movies S2 and S3). Interestingly, the 3D-reconstituted image of the tree includes main stem bronchus, bronchi, bronchioles, and even alveoli structures. We next analyzed whole-kidney images from the same mKate2 KI mouse. Renal cortex, medulla, and pelvis were clearly distinguished and annotated with characteristic signal patterns of SYTO16 and mKate2 (Figure 6C and Movie S4). We further analyzed whole-liver images from the same mKate2 KI mouse (Figure 6D and Movie S5). We extracted two vessel structures inside of the image, which were characterized

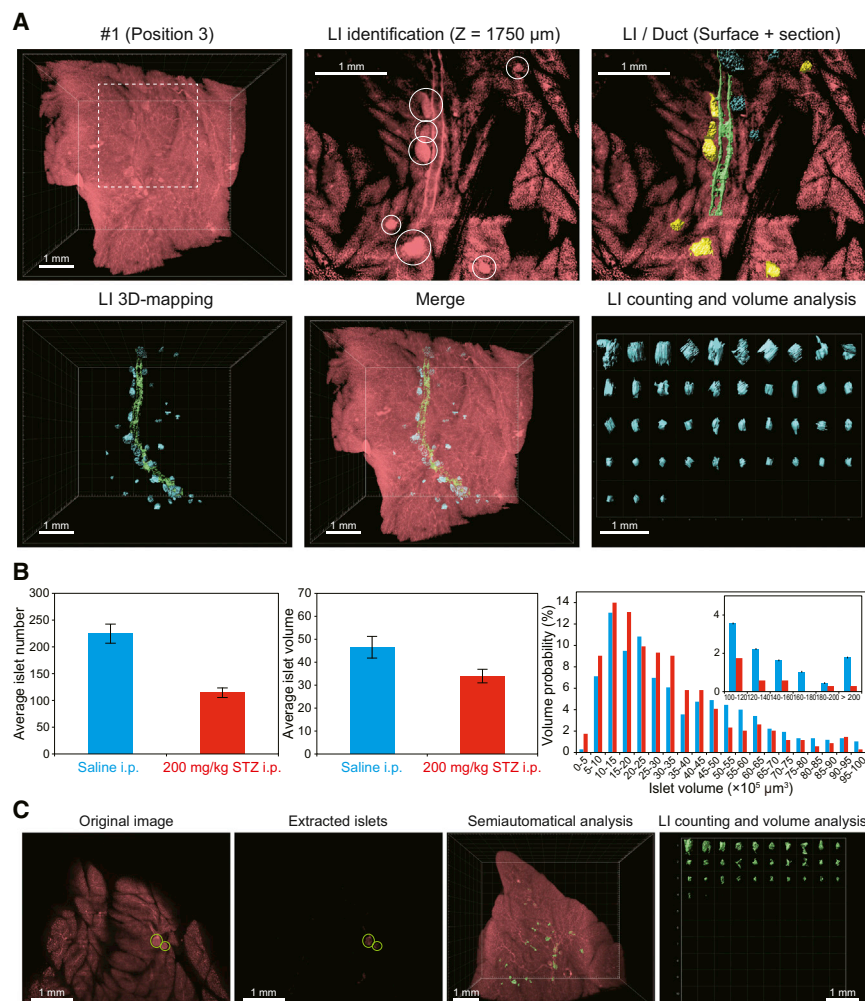


**Figure 5. CUBIC Is Applicable to the 3D Pathology of Langerhans Islets in the Diabetic Pancreas**

(A) The procedures for image analysis of LIs in pancreases. First, LIs in each X-Y plane image were manually identified. Seven LIs (white circles) were identified in the center-top panel. Then, these LIs were visualized in a 3D image with surface analysis on the Imaris software. In the upper-right panel, the seven LIs (yellow) are in the plane. Four other LIs (blue) are not in the same plane. The pancreatic duct (green) is also indicated. The spatial distribution of LIs (blue) as well as a pancreatic duct (green) is displayed in the lower-left and lower-center panels. Finally, LI counting and volume analysis were conducted on the Imaris software, shown in the lower-right panel.

(B) Statistical analysis of LIs in the whole pancreas from control mice ( $n = 3$ ) and diabetes mice ( $n = 3$ ). Data represent the average  $\pm$  SE. The average number of LIs was significantly reduced by the onset of diabetes (left,  $p = 0.005$ ). The differences of average LI volume between diabetic and healthy mice were also marginally significant (center,  $p = 0.09$ ), which is consistent with the observed reduction in the existence probability of larger LIs in diabetic mice (right,  $> 1.0 \times 10^7 \mu\text{m}^3$ ).

(C) Computational, semi-automated identification of LIs. Position 1 image of #1 mouse was used. (Left and center) Raw and processed image with extracted islets (green circles) at plane 80. (Right) Reconstituted 3D image with all identified islets. See also [Table S1](#).

by high and low SYTO 16 signals, and were thus identified as hepatic arteries and portal veins, respectively. Finally, we extended similar anatomical analysis to whole-body images of PI-stained CAG-EGFP Tg P1 mouse ([Figure 3](#)). Each organ inside of the chest and upper abdomen were clearly visualized ([Figure S8A](#) and [Movie S6](#)) with their inside structures, such as a bronchial tree in the lung ([Figure S8B](#)), vascular structures in the liver ([Figure S8C](#)), villi in the intestine ([Figure S8D](#)), and spatial relations of esophagus and esophageal gland ([Figure S8E](#)). These results suggest that CUBIC enables 3D anatomy of various organs even in whole-body images, which will provide a versatile platform for systems-level elucidation of cellular circuits underlying the physiology and pathology of various organs of interest.

### CUBIC Is Applicable to 3D Immunohistochemistry of Various Organs

Another challenge for establishing whole-organ imaging is the development of 3D immunohistochemistry (3D-IHC). In our previous work, we have demonstrated that CUBIC was applicable to the 3D-IHC using large blocks of brain tissue ([Susaki et al., 2014](#)). According to the protocol, we performed 3D-IHC of

nuclear-stained whole-organ samples ([Figure 7A](#)). Organ samples with CB-Perfusion were subjected to CUBIC-1 treatment, followed by 3D-IHC with antibodies to two proteins expressed in the organs. We used  $\alpha$ -smooth muscle actin ( $\alpha$ -SMA) antibody to label the heart, stomach, and intestine and pan-cytokeratin antibody to the lung. After immunostaining, organ samples were treated with CUBIC-2 for several hours to 1 day, and the resulting samples were observed with LSMF. The immunostained signals were detected over 1 mm depth and were visualized as 3D-reconstituted images ([Figure 7](#)). In the heart, the immunofluorescence signal for  $\alpha$ -SMA antibody clearly highlighted vascular structures ([Figure 7B](#)). Epithelial cells in the lung were visualized by immunostaining with the antibody to pan-cytokeratin ([Figure 7C](#)). Previously reported staining pattern of pan-cytokeratin was recapitulated by CUBIC-based 3D-IHC ([Xiang et al., 2007](#)).  $\alpha$ -SMA antibody also visualized smooth muscular cells in the stomach and intestine ([Figures 7D](#) and [7E](#)). The CUBIC protocol is thus applicable to the 3D-IHC of various organs.

### DISCUSSION

#### Aminoalcohols in CUBIC Enable Decolorization of Blood

Almost all animals are not transparent because their body is composed of RI-mismatched materials as well as light-absorbing

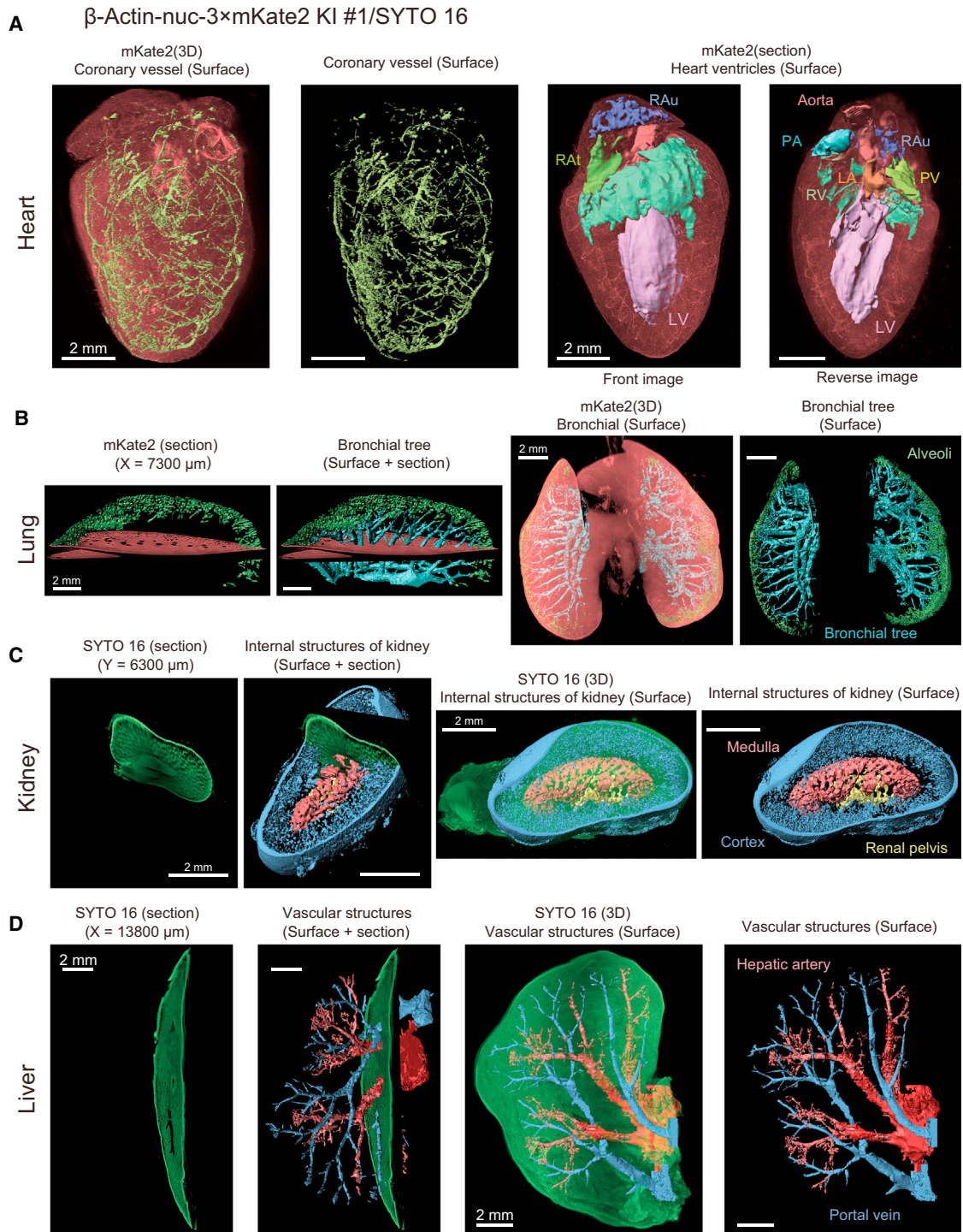


**Figure 6. CUBIC Is Applicable to the 3D Anatomy of Various Organs**

Extraction of internal structures was performed with surface analysis of Imaris software. The reconstituted 3D images of the heart (A), lung (B), kidney (C), and liver (D) from the SYTO 16-stained  $\beta$ -actin-nuc-3  $\times$  mKate2 KI mouse (8-week-old) in Figure 4 were used. After surface extraction by the software, each structure was manually curated and extra surface signals were eliminated.

(A) Structural identification of coronary vessels and ventricles in the heart. Contiguous mKate2 signals with high or low intensity within the heart were extracted as coronary vessels (left two panels) or ventricles (right two panels). RAu, right auricle; RAT, right atrium; RV, right ventricle; LA, left atrium; LV, left ventricle; PA, pulmonary artery; PV, left ventricle.

(legend continued on next page)

pigments. Although a number of tissue-clearing methods (BABB, THF-DBE, Scale, SeeDB, *ClearT*) and protocols (3DISCO, CLARITY, PACT-PARS) have been developed, the importance of tissue decolorization may have been overlooked because these methods were mainly optimized for pigment-less brains and hence focused on the adjustment of mismatched RIs (Becker et al., 2012; Chung et al., 2013; Dodt et al., 2007; Ertürk et al., 2012; Hama et al., 2011; Ke et al., 2013; Kuwajima et al., 2013; Yang et al., 2014). However, when applied to whole body, thick tissues may block photons in the visible region due to the absorbance by endogenous pigments. Animals genetically lacking endogenous pigments have see-through bodies such as the medaka, in which superficial organs can be visualized across body surfaces (Ohshima et al., 2013; Wakamatsu et al., 2001). Therefore, to visualize detailed structures in deeper organs by single-photon excitation microscopy, we must overcome the light absorbance by heme, which is one of the most abundant chromophores in the body (Faber et al., 2003; Weissleder, 2001), in addition to light scattering by mismatched RIs. In the previous study, we demonstrated that aminoalcohols in CUBIC cocktails significantly enhanced whole-brain clearing via homogenizing mismatched RIs (Susaki et al., 2014). In this study, we discovered another unexpected chemical nature of aminoalcohols: tissue decolorization. Q bands (~500–700 nm) of heme in erythrocytes treated with aminoalcohol #10 or CUBIC-1 reagent were considerably changed from those of hemoglobin-bound form (Figure 1C). These results imply that the aminoalcohols could be tightly bound to heme porphyrin instead of oxygen and histidine in hemoglobin, which may facilitate heme release and explain the unexpected expansion of the effective pH window for heme release. Additionally, the buffering capability of aminoalcohol #10 in moderately basic conditions should also contribute to the decolorizing performance (Figures 1E and 1F). Importantly, the buffering capability of aminoalcohol #10 is exerted in moderately basic conditions, which is the optimal pH range for the fluorescence signal from GFP-related fluorescence proteins (Haupts et al., 1998). In fact, treatment of individual organs by CUBIC reagents led to much higher transmittance in the visible region than that of organs treated by other reagents (Figure S2B), whereas CUBIC reagents could preserve the fluorescence signal from various kinds of GFP-related fluorescence proteins (Figure S6).

### CUBIC Enables Whole-Body Clearing and Whole-Body Imaging with Single-Cell Resolution

In this study, we demonstrated that the CB-Perfusion protocol, which enabled both tissue decolorization and adjustment of mismatched RIs, achieved the visualization of chest and abdominal backbones through internal organs as well as bones of limbs

through soft tissues from both ventral and dorsal sides of the adult and infant mice (Figure 2B). We also demonstrated that the CB-Perfusion protocol achieved whole-body (Figure 3) and whole-organ (Figure 4) imaging with single-cell resolution. We note that CUBIC is also compatible with other protocols. For example, we previously demonstrated that CUBIC reagents are applicable to clear acrylamide-gel-embedded samples prepared according to the CLARITY protocol (Susaki et al., 2014). Therefore, we expect that another CLARITY-inspired protocol, PARS, can be a useful fixation method for the endogenous molecules before CUBIC treatment. Because the PARS method is based on the intracardiac circulation of detergents (Yang et al., 2014), similar to the CB-Perfusion protocol, additional circulation of decolorizing medium (CUBIC cocktails) might increase transparency in the PARS method.

There are still some fundamental technical challenges remaining in both whole-body clearing and whole-body imaging. Although in this study CUBIC cocktails facilitated the transparency of internal organs and soft tissues for the infant and adult mice body by tissue decolorization, these clearing reagents are not effective for bones. Conventionally, decalcification is rendered by the continuous immersion of acids (such as formic acids) or chelating agents (such as EDTA) (Mack et al., 2014). Therefore, the combination of effective chelating solution with CUBIC cocktails might provide further decalcification properties for the current chemical cocktail. Alternatively, larger chemical screening for tissue-clearing reagents (Susaki et al., 2014) could afford a series of alternative candidates for tissue- and/or bone-clearing reagents that may provide more clearing potency with fewer drawbacks. In whole-body imaging, further optimization of LSFM setup is also required to seamlessly capture whole-body images of adult mice. Because the movable range of the stage was limited in the currently existing LSFM setup, the largest field of view corresponded to a P1 mouse. An entire adult mouse is much thicker, wider, and longer than the body of an infant mouse. Thus, extension of focus depth in the illuminated light-sheet, expansion of the movable range of the stage, and seamless tiling of the reconstituted images should be improved in future LSFM setups.

### CUBIC Is Applicable to 3D Pathology, Anatomy, and Immunohistochemistry

Whole-body and whole-organ imaging with single-cell resolution will play a fundamental role in achieving 3D studies of pathology and anatomy, which will aid in systems-level elucidation of cellular mechanisms underlying abnormal and normal body states. In this study, we applied CUBIC-based whole-body clearing and LSFM-based whole-organ/whole-body imaging to achieve 3D pathology, anatomy, and immunohistochemistry.

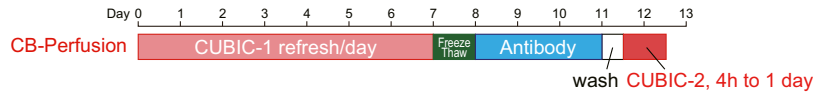
(B) Structural identification of the bronchial tree (light blue) and peripheral alveoli (green) in the lung. Contiguous mKate2 signals with moderate intensity within or on the edge of the lung were extracted as the bronchial tree or alveoli, distinguished by their values of surface area.

(C) Structural identification of renal cortex, medulla, and pelvis in the kidney. High-intensity signals in SYTO 16 channel and high- or low-intensity signals of mKate2 channel were extracted as the cortex, medulla, or pelvis, respectively.

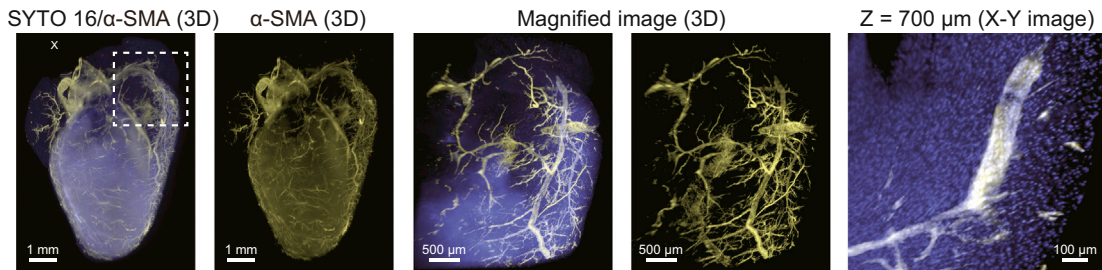
(D) Structural identification of vessels in the liver. Two types of vascular structures (with or without high-concentrated nuclei signals around the vessel) were distinguished. Contiguous SYTO 16 signals with low or moderate intensity were extracted as the portal vein (blue) or wall of the hepatic artery (red), respectively. In mKate2 channel, similar contiguous signals with low intensity were also extracted and merged with the hepatic artery structure (red).

See also Figures S7 and S8.

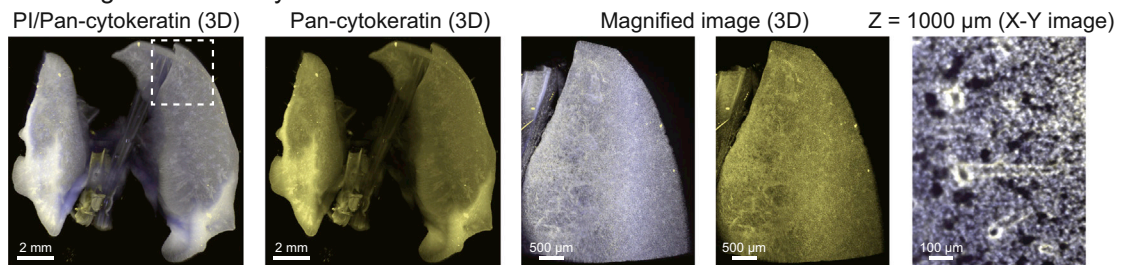
### A Whole-organ immunostaining protocol with CB-Perfusion



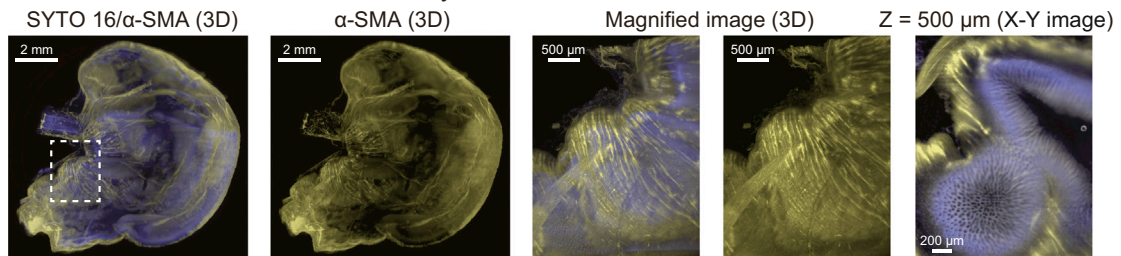
### B Heart SYTO 16/anti- $\alpha$ -SMA Cy3



### C Lung PI/anti-Pan-cytokeratin FITC



### D Stomach SYTO 16/anti- $\alpha$ -SMA Cy3



### E Intestine SYTO 16/anti- $\alpha$ -SMA Cy3

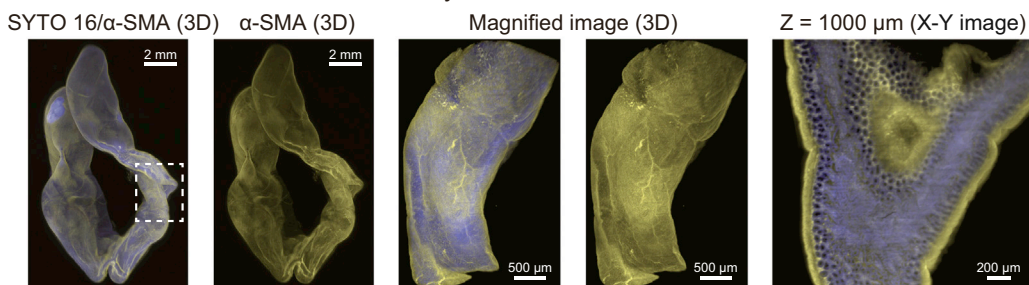


#### Figure 7. CUBIC Is Applicable to the 3D Immunohistochemistry of Various Organs

(A) CUBIC protocol for 3D immunohistochemistry (3D-IHC) of CB-perfused various organs. The reconstituted 3D and section images of a SYTO 16- or PI-stained heart (B), lung (C), stomach (D), and intestine (E) from C57BL/6N mouse (11-week-old) immunostained with Cy3-conjugated anti- $\alpha$ -SMA for heart, stomach, and intestine or FITC-conjugated anti-pan cytokeratin for lung were acquired with LSM. Magnified 3D images and raw X-Y section images are at the indicated positions.

As a model case study, we analyzed entire pancreases in diabetic and normal mice to reveal the volume distribution of LIs between diabetic and healthy mice. As expected, the total number

and volume distribution of LIs were significantly different between normal and diabetic mice (Figure 5). We also note that larger LIs tend to be localized along pancreatic ducts and

are more susceptible to  $\beta$  cell impairment induced by STZ administration.

The application of whole-body and whole-organ imaging techniques is not limited to the pancreas but can be extended to other organs. In this study, we demonstrated that 3D anatomy is feasible for other medically important structures from whole-organ (Figure 6) or whole-body images (Figure S8) such as coronary vessels in the heart; the bronchial tree in the lungs; glomeruli distributed through the cortex and the medullary rays in the kidney, artery, and vein networks of the liver; and villi in the intestine. Although such medically important structures are annotated manually in this study, automated or semi-automated extraction of medically important anatomical structures will facilitate 3D pathology and anatomy in future. As a pilot study, we attempted and succeeded in semi-automated extraction of medically important anatomical structures in abdominal and chest organs such as IIs in the pancreas (Figure 5C) and the coronary vessels in the heart (Figure S7B). We also note that CUBIC application is not limited to transgenic mice with fluorescence reporter (Figure 7). Because 3D-IHC is compatible with CUBIC, this whole-organ and whole-body clearing technique can be widely applied to various mice without fluorescence reporter. When combined with informatics as well as immunohistochemistry, CUBIC will thus contribute to the systems-level elucidation of cellular mechanisms underlying the generation and progression of diseases especially with stochastic and proliferative processes such as autoimmune diseases. New research fields such as organism-level systems biology based on whole-body imaging with single-cell resolution lie ahead.

## EXPERIMENTAL PROCEDURES

Additional details are available in the [Extended Experimental Procedures](#).

### Decolorization of the Blood by Aminoalcohols in CUBIC Cocktails

PFA-fixed blood was thoroughly mixed with each chemical, and resultant pellet and supernatant were imaged by bright-field microscopy. For taking visible spectra data, erythrocytes were mixed with each chemical and incubated at 37°C overnight. The mixtures and supernatant were diluted 10-fold with each chemical. The visible spectra of samples was recorded by UV/Vis spectrometer (JASCO, V-550, Japan). In the decoloring capacity test, the mixtures of erythrocytes and each chemical with different mixing ratios (erythrocyte/chemical = 0.01 to 0.20) were incubated at 37°C overnight. Bright-field images of these samples were captured. In the pH dependency of heme release, erythrocytes were mixed with each chemical and incubated at 37°C for 1 hr. The OD575 and OD600 values of the mixtures were measured with the PowerWave XS and the attached operation software (Bio-Tek).

### Mice

The  $\beta$ -actin-*mKate2* knockin mouse ( $\beta$ -actin-CAG-nuc-3  $\times$  *mKate2*) strain was established in our laboratory. We also used the R26-H2B-EGFP KI (CDB0238K) (Abe et al., 2011), Thy1-YFP-H Tg (Feng et al., 2000), C57BL/6-Tg (CAG-EGFP) (Okabe et al., 1997), BALB/cA<sup>J</sup>cl-*nu/nu*, and wild-type C57BL/6N mouse strains. We fed DietGel Recovery (LSG Corporation, 72-06-5022, Japan) to mice for imaging the intestine. Diabetes was induced in male C57BL/6N mice at 8 weeks by a single intraperitoneal administration of saline or 10 mg/ml streptozotocin (total 200 mg/kg, Wako Pure Chemical Industries, 197-15153) at day 0. Blood glucose values were measured by a blood glucose monitor (GLUCOCARD G Black; ARKRAY) after fasting for 6 hr at day 0 and 4. Mice with blood glucose levels over 300 mg/dl ( $n = 5$ ) at day 4 and saline-administered mice ( $n = 4$ ) were used for clearing with CUBIC perfusion and PI staining. All experimental procedures and housing conditions

were approved by the Animal Care and Use Committee of Graduate School of Medicine, the University of Tokyo or by the Animal Care and Use Committee of the RIKEN Kobe Institute, and all of the animals were cared for and treated humanely in accordance with the Institutional Guidelines for Experiments Using Animals.

### The CUBIC Protocol and Other Clearing Methods

Two CUBIC reagents were prepared as previously reported (Susaki et al., 2014). For preparation of CUBIC-treated (non-perfused) samples, the fixed organs were immersed in CUBIC-1 reagent for 5 days and were further immersed in CUBIC-2 reagent. To make CUBIC-1 reagent penetrate throughout the whole body, we also performed the CB-Perfusion protocol. The anesthetized adult mouse was perfused with 10 ml of 10 U/ml of heparin in PBS, 150 ml of 4% (w/v) PFA in PBS, 20 ml of PBS (to wash out PFA), and 20 ml of 50% (v/v) CUBIC-1 reagent (1:1 mixture of water: CUBIC-1) in this order via left ventricle of the heart. (The protocol was slightly modified for infant mice.) The resulted whole animal or excised organs were continuously immersed in CUBIC-1 reagent for 5 days to several weeks. Organs were further immersed in CUBIC-2 reagent. These samples were stained with nucleic acid stains PI (Life Technologies, P21493) or SYTO 16 (Life Technologies, S7578), when indicated. We also performed SeeDB standard protocol (Ke et al., 2013) and ScaleA2 and ScaleB4 protocol (Hama et al., 2011). Light transmittance was measured with an integrating sphere (Spectral Haze Meter SH 7000, Nippon Denshoku Industries).

### Microscopy and Image Analysis

Whole-body and organ fluorescence images were acquired with light-sheet fluorescence microscopy (LSFM) (Ultramicroscope, LaVision BioTec, Germany) as reported previously (Dodt et al., 2007; Susaki et al., 2014). All raw image data were collected in a lossless 16-bit TIFF format. 3D-rendered images were visualized, captured, and analyzed with Imaris software (version 7.6.4 and 7.7.1, Bitplane). Blind 3D deconvolution for a set of our LSFM z stack images was performed with software AutoQuant X3 (Media Cybernetics). Anatomical structures and LI quantification were performed with surface analysis of Imaris software. Automated detections of anatomical structure were performed with Fiji (Schindelin et al., 2012) and using a filtering method implemented in C++.

## SUPPLEMENTAL INFORMATION

Supplemental Information includes Extended Experimental Procedures, eight figures, one table, and six movies and can be found with this article online at <http://dx.doi.org/10.1016/j.cell.2014.10.034>.

## AUTHOR CONTRIBUTIONS

H.R.U., K.T., and S.I.K. designed the study. K.T., S.I.K., and T.Q.S. performed most of the experiments. E.A.S. developed CB-Perfusion protocol. D.P. contributed to the image informatics. M.U.-T. and H.U. produced  $\beta$ -actin-nuc-3  $\times$  *mKate2* KI mice. All authors discussed the results and commented on the manuscript text.

## ACKNOWLEDGMENTS

We thank the lab members at RIKEN CDB, QBIC, and The University of Tokyo, in particular, H. Yukinaga, J. Hara, J. Yoshida, C. Imai, and Y. Niwa for their kind help in preparing the materials; A. Millius for reviewing and editing the manuscript; K. Matsumoto for helpful suggestions in developing the CB-Perfusion protocol; Y. Abe, T. Sengoku, and S. Kondo for their kind help in developing the CB-Perfusion protocol and transmittance evaluation; and S. Shoi for his kind help in statistical analysis. We also thank T. Abe and H. Kiyonari for providing materials for targeting vectors and R26-H2B EGFP mice; LARGE, RIKEN CDB for housing the mice; D. Asanuma and K. Hirose for their kind help in measuring visible spectra; H. Sekiya, K. Kanemaru, D. Ino, J. Suzuki, K. Miyazono, S. Ehata, K. Takahashi, H. Takayanagi, S. Sawa, G. Matteo, Y. Mori, and Y. Yoshioka for their kind comments and suggestions; and Media

Cybernetics for supporting the usage of AutoQuant X3. This work was supported by the Program for Innovative Cell Biology by Innovative Technology and the Brain Mapping by Integrated Neurotechnologies for Disease Studies (Brain/MINDS) from the Ministry of Education, Culture, Sports, Science and Technology (MEXT) of Japan, a Grant-in-Aid for Scientific Research (S) (grant no. 25221004), a Grant-in-Aid for Scientific Research on Innovative Areas (grant no. 23115006), and a Grant-in-Aid JSPS Fellows (grant no. 26-1180) from MEXT/Japan Society for the Promotion of Science (JSPS), the strategic programs for R&D (President's discretionary fund) of RIKEN, an intramural Grant-in-Aid from the RIKEN Center for Developmental Biology and RIKEN Quantitative Biology Center, a grant from Core Research for Evolutional Science and Technology (CREST), Japan Science and Technology Agency (JST), a Grant-in-Aid from Japan Foundation for Applied Enzymology, a Grant-in-Aid from the Shimabara Science Promotion Foundation, and by the RIKEN Foreign Postdoctoral Researcher Program.

Received: August 18, 2014  
 Revised: September 30, 2014  
 Accepted: October 11, 2014  
 Published: November 6, 2014

## REFERENCES

- Abe, T., Kiyonari, H., Shioi, G., Inoue, K.I., Nakao, K., Aizawa, S., and Fujimori, T. (2011). Establishment of conditional reporter mouse lines at ROSA26 locus for live cell imaging. *Genesis* 49, 579–590.
- Alanentalo, T., Asayesh, A., Morrison, H., Lorén, C.E., Holmberg, D., Sharpe, J., and Ahlgren, U. (2007). Tomographic molecular imaging and 3D quantification within adult mouse organs. *Nat. Methods* 4, 31–33.
- Alnami, A.A., Zeedi, B., Qadri, S.M., and Ashraf, S.S. (2008). Oxyradical-induced GFP damage and loss of fluorescence. *Int. J. Biol. Macromol.* 43, 182–186.
- Becker, K., Jährling, N., Saghafi, S., Weiler, R., and Dodt, H.U. (2012). Chemical clearing and dehydration of GFP expressing mouse brains. *PLoS ONE* 7, e33916.
- Chudakov, D.M., Matz, M.V., Lukyanov, S., and Lukyanov, K.A. (2010). Fluorescent proteins and their applications in imaging living cells and tissues. *Physiol. Rev.* 90, 1103–1163.
- Chung, K., Wallace, J., Kim, S.Y., Kalyanasundaram, S., Andalman, A.S., Davidson, T.J., Mirzabekov, J.J., Zalocusky, K.A., Mattis, J., Denisin, A.K., et al. (2013). Structural and molecular interrogation of intact biological systems. *Nature* 497, 332–337.
- Dodt, H.U., Leischner, U., Schierloh, A., Jährling, N., Mauch, C.P., Deininger, K., Deussing, J.M., Eder, M., Ziegglänsberger, W., and Becker, K. (2007). Ultramicroscopy: three-dimensional visualization of neuronal networks in the whole mouse brain. *Nat. Methods* 4, 331–336.
- Ertürk, A., Becker, K., Jährling, N., Mauch, C.P., Hojer, C.D., Egen, J.G., Hellal, F., Bradke, F., Sheng, M., and Dodt, H.U. (2012). Three-dimensional imaging of solvent-cleared organs using 3DISCO. *Nat. Protoc.* 7, 1983–1995.
- Faber, D.J., Mik, E.G., Aalders, M.C., and van Leeuwen, T.G. (2003). Light absorption of (oxy-)hemoglobin assessed by spectroscopic optical coherence tomography. *Opt. Lett.* 28, 1436–1438.
- Feng, G.P., Mellor, R.H., Bernstein, M., Keller-Peck, C., Nguyen, Q.T., Wallace, M., Nerbonne, J.M., Lichtman, J.W., and Sanes, J.R. (2000). Imaging neuronal subsets in transgenic mice expressing multiple spectral variants of GFP. *Neuron* 28, 41–51.
- Hama, H., Kurokawa, H., Kawano, H., Ando, R., Shimogori, T., Noda, H., Fukami, K., Sakaue-Sawano, A., and Miyawaki, A. (2011). *Scale*: a chemical approach for fluorescence imaging and reconstruction of transparent mouse brain. *Nat. Neurosci.* 14, 1481–1488.
- Haupts, U., Maiti, S., Schwille, P., and Webb, W.W. (1998). Dynamics of fluorescence fluctuations in green fluorescent protein observed by fluorescence correlation spectroscopy. *Proc. Natl. Acad. Sci. USA* 95, 13573–13578.
- Ke, M.T., Fujimoto, S., and Imai, T. (2013). SeeDB: a simple and morphology-preserving optical clearing agent for neuronal circuit reconstruction. *Nat. Neurosci.* 16, 1154–1161.
- Keller, P.J., and Dodt, H.U. (2012). Light sheet microscopy of living or cleared specimens. *Curr. Opin. Neurobiol.* 22, 138–143.
- King, A.J.F. (2012). The use of animal models in diabetes research. *Br. J. Pharmacol.* 166, 877–894.
- Kristinsson, H.G., and Hultin, H.O. (2004). Changes in trout hemoglobin conformations and solubility after exposure to acid and alkali pH. *J. Agric. Food Chem.* 52, 3633–3643.
- Kuwajima, T., Sitko, A.A., Bhansali, P., Jurgens, C., Guido, W., and Mason, C. (2013). *Clear<sup>T</sup>*: a detergent- and solvent-free clearing method for neuronal and non-neuronal tissue. *Development* 140, 1364–1368.
- Mack, S.A., Maltby, K.M., and Hilton, M.J. (2014). Demineralized murine skeletal histology. *Methods Mol. Biol.* 1130, 165–183.
- Niwa, H., Yamamura, K., and Miyazaki, J. (1991). Efficient selection for high-expression transfectants with a novel eukaryotic vector. *Gene* 108, 193–199.
- Ohshima, A., Morimura, N., Matsumoto, C., Hiraga, A., Komine, R., Kimura, T., Naruse, K., and Fukamachi, S. (2013). Effects of body-color mutations on vitality: an attempt to establish easy-to-breed see-through medaka strains by outcrossing. *G3* 3, 1577–1585.
- Okabe, M., Ikawa, M., Kominami, K., Nakanishi, T., and Nishimune, Y. (1997). 'Green mice' as a source of ubiquitous green cells. *FEBS Lett.* 407, 313–319.
- Schindelin, J., Arganda-Carreras, I., Frise, E., Kaynig, V., Longair, M., Pietzsch, T., Preibisch, S., Rueden, C., Saalfeld, S., Schmid, B., et al. (2012). Fiji: an open-source platform for biological-image analysis. *Nat. Methods* 9, 676–682.
- Shcherbo, D., Murphy, C.S., Ermakova, G.V., Solovieva, E.A., Chepurnykh, T.V., Shcheglov, A.S., Verkhusha, V.V., Pletnev, V.Z., Hazelwood, K.L., Roche, P.M., et al. (2009). Far-red fluorescent tags for protein imaging in living tissues. *Biochem. J.* 418, 567–574.
- Spalteholz, W. (1914). Über das Durchsichtigmachen von menschlichen und tierischen Präparaten (Leipzig: S. Hierzel).
- Steinke, H., and Wolff, W. (2001). A modified Spalteholz technique with preservation of the histology. *Ann. Anat.* 183, 91–95.
- Susaki, E.A., Tainaka, K., Perrin, D., Kishino, F., Tawara, T., Watanabe, T.M., Yokoyama, C., Onoe, H., Eguchi, M., Yamaguchi, S., et al. (2014). Whole-brain imaging with single-cell resolution using chemical cocktails and computational analysis. *Cell* 157, 726–739.
- Tanaka, K.F., Matsui, K., Sasaki, T., Sano, H., Sugio, S., Fan, K., Hen, R., Nakai, J., Yanagawa, Y., Hasuwa, H., et al. (2012). Expanding the repertoire of optogenetically targeted cells with an enhanced gene expression system. *Cell Rep.* 2, 397–406.
- Teale, F.W. (1959). Cleavage of the haem-protein link by acid methylethylketone. *Biochim. Biophys. Acta* 35, 543.
- Tomer, R., Khairy, K., and Keller, P.J. (2011). Shedding light on the system: studying embryonic development with light sheet microscopy. *Curr. Opin. Genet. Dev.* 21, 558–565.
- Tomer, R., Ye, L., Hsueh, B., and Deisseroth, K. (2014). Advanced CLARITY for rapid and high-resolution imaging of intact tissues. *Nat. Protoc.* 9, 1682–1697.
- Wakamatsu, Y., Pristiyazhnyuk, S., Kinoshita, M., Tanaka, M., and Ozato, K. (2001). The see-through medaka: a fish model that is transparent throughout life. *Proc. Natl. Acad. Sci. USA* 98, 10046–10050.
- Weissleder, R. (2001). A clearer vision for *in vivo* imaging. *Nat. Biotechnol.* 19, 316–317.
- Xiang, Y.Y., Wang, S., Liu, M., Hirota, J.A., Li, J., Ju, W., Fan, Y., Kelly, M.M., Ye, B., Orser, B., et al. (2007). A GABAergic system in airway epithelium is essential for mucus overproduction in asthma. *Nat. Med.* 13, 862–867.
- Yang, B., Treweek, J.B., Kulkarni, R.P., Deverman, B.E., Chen, C.K., Lubeck, E., Shah, S., Cai, L., and Gradinaru, V. (2014). Single-cell phenotyping within transparent intact tissue through whole-body clearing. *Cell* 158, 945–958.

## EXTENDED EXPERIMENTAL PROCEDURES

**Decolorization of the Blood by Aminoalcohols in CUBIC Cocktails**

We hypothesized that CUBIC-1 reagent could solubilize and elute endogenous heme from blood-infused tissues. To test this hypothesis, we first investigated whether CUBIC reagents can directly decolorize blood. PFA-fixed blood was prepared by equivalent mixing of murine blood and 8% PFA-PBS, and incubated at 37°C overnight. Erythrocytes were purified by centrifugation of incoagulable blood including 1 mg/ml EDTA at 3000 rpm for 30 min, supernatant wasting, and followed by three-times washing with 1 ml PBS and centrifugation at 3000 rpm for 30 min. Both blood samples were stored at 4°C. In the decoloring experiments of PFA-fixed blood (Figures 1A and 1B), PFA-fixed blood (100  $\mu$ l) was thoroughly mixed with each chemical [400  $\mu$ l of PBS, CUBIC-1 reagent, 25 wt% *N,N,N',N'*-tetrakis(2-hydroxypropyl)ethylenediamine (aminoalcohol #10), 25 wt% urea, 15 wt% Triton X-100, 0.01 M NaOH, the mixture of 25 wt% urea and 15 wt% Triton X-100, 25 wt% glycerol, or the mixture of 25 wt% urea, 25 wt% glycerol, and 15 wt% Triton X-100 (modified ScaleA2)], and then immediately centrifuged at 15000 rpm for 5 min. Supernatant was collected and pellet was washed with each chemical (500  $\mu$ l) three times (we noted that since mixing efficiency is critical for the clearing performance in the washing step, the mixture should be not only mixed by a vortex mixer, but also vigorously stirred by the small spatula). The pellet was suspended in each chemical (500  $\mu$ l), and transferred in the dish. The collected supernatant (500  $\mu$ l) was also transferred in the dish. Bright-field images of these samples were captured. As a result, aminoalcohol #10 alone, but not other reagents, is sufficient to decolorize the blood (Figure 1A). We also found that PFA-fixed blood could not be decolorized by glycerol, a mixture of urea and Triton X-100, or modified ScaleA2 (the mixture of glycerol, urea, and Triton X-100) (Figure 1B), suggesting that aminoalcohol #10 in CUBIC-1 reagent is the active reagent in blood clearing. We also note that the decolorizing capability of aminoalcohol #10 is not solely dependent on its high pH because PFA-fixed blood was not efficiently decolorized by highly basic solution (0.01 M NaOH, initial pH = 12). Therefore, the blood decolorizing nature of aminoalcohol #10 in a moderately basic condition originates from its chemical property.

We next investigated what kind of olive-green molecule was eluted from the blood into the supernatant. Thus, the visible spectra of chemically-treated blood samples were recorded by UV/Vis spectrometer (JASCO, V-550) (Figures 1C, 1D, and S1A). Erythrocytes (5  $\mu$ l) were mixed with each chemical (PBS, 0.1 M NaOH, 25 wt% #10, or CUBIC-1 reagent), and incubated at 37°C overnight. The mixtures and supernatant from CUBIC-1- or #10-treated PFA-fixed blood were diluted 10-fold with each chemical. We also prepared 10  $\mu$ M of hemin (Tokyo Chemical Industry), 10  $\mu$ M of biliverdin (Sigma-Aldrich), and 100  $\mu$ M of iron(II) chloride (Nacalai Tesque), solubilized with CUBIC-1 reagent or #10. The normalized spectra of the erythrocyte and supernatant overlapped almost completely with hemin solutions in aminoalcohol #10 or CUBIC-1, which suggests that heme is released from hemoglobin in erythrocytes when treated by aminoalcohol #10 or the CUBIC-1 reagent (Figures 1D and S1A).

Aminoalcohol #10 in the CUBIC-1 reagent can solubilize and elute the heme in the blood more efficiently than highly basic solution (0.01 M NaOH, initial pH = 12) (Figure 1A). What kind of chemical property in aminoalcohol #10 enables heme elution at moderate pH? As shown in Figure 1A, we noticed that the pH variations were relatively small between the original liquid and the subsequent supernatant for samples treated by aminoalcohol #10 and CUBIC-1 reagent when compared with highly basic solution (0.01 M NaOH, initial pH = 12). These results indicate that aminoalcohol #10 has buffering capacity at moderately basic conditions. To directly test the buffering capacity of these reagents, 50 g of CUBIC-1 reagent, 25 wt% aminoalcohol #10, 25 wt% glycerol containing 0.01 M NaOH, 25 wt% urea containing 0.01 M NaOH, 15 wt% Triton X-100 containing 0.01 M NaOH, or 0.01 M NaOH were titrated with 1 M HCl (Figure S1B). pH was measured by pH meter (HORIBA, LAQUAtwin). As a result, aminoalcohol #10 and CUBIC-1 reagent have buffering capacity in pH 9-11 whereas other reagents did not.

If buffering capacity in basic pH is critical for the decolorizing capability, we predicted that a basic solution containing 0.01 M NaOH, which usually elutes heme from hemoglobin, will lose its decolorizing capability at a higher concentration of erythrocytes because the higher concentration of cells will shift the pH from basic to neutral. To test this prediction, we prepared a mixture of erythrocytes and these chemicals at different ratios (Figure 1E). In the experiment, the mixtures (200  $\mu$ l) of erythrocytes and each chemical (CUBIC-1 reagent, 25 wt% #10, 25 wt% glycerol containing 0.01 M NaOH, 25 wt% urea containing 0.01 M NaOH, 15 wt% Triton X-100 containing 0.01 M NaOH, or 0.01 M NaOH) with different mixing ratio (erythrocyte/chemical = 0.01 to 0.20) were incubated at 37°C overnight. Bright-field images of these samples were captured. The OD575 and OD600 values of the mixtures were measured with the PowerWave XS and the attached operation software (Bio-Tek). Since the absorbance was saturated at erythrocyte/chemical ratio = 0.20 in Figure 1E, the OD600/OD575 values at this ratio were not collected in Figure S1C. These results quantitatively confirmed that aminoalcohol #10 in the CUBIC-1 reagent can efficiently promote heme release regardless of the erythrocyte/chemical ratio, and work as a decolorizing buffer at moderate basic pH.

Since previous studies reported that heme can be released only in highly basic ( $\geq$  pH 11) or acidic ( $\leq$  pH 2) conditions (Kristinsson and Hultin, 2004; Teale, 1959), the remaining question is whether the decolorizing capability of aminoalcohol #10 in the CUBIC-1 reagent occurs only in highly basic conditions (pH > 11), or can occur in less basic conditions (pH < 11), in which GFP-related fluorescence proteins emit stronger fluorescence signal (Haupts et al., 1998). Thus, we evaluated the pH dependence on the efficiency of heme release for 25 wt% aminoalcohol #10, CUBIC-1 reagent, 25 wt% tris(hydroxymethyl)aminomethane (Tris), and NaOH aqueous solution, respectively (Figure 1F). pHs of CUBIC-1 reagent, #10, Tris solutions were adjusted by acidification with HCl or basification with NaOH. Erythrocytes (5  $\mu$ l) were mixed with each chemical (CUBIC-1 reagent, 25 wt% #10, 25 wt% Tris, or NaOH solution), and

incubated at 37°C for 1 hr. The OD575 and OD600 values of the mixtures were measured with the PowerWave XS. Haupts U. et al. revealed that GFP fluorescence signals were more intensified in the moderate basic condition (pH 8–11) than in the neutral condition (pH 7.0) (Haupts et al., 1998). In our previous manuscript, we also demonstrated that GFP signals in some of 10 wt% basic aminoalcohols were higher than those in PBS (pH 7.4) (Susaki et al., 2014). Therefore, moderate basic condition between pH 8 to 11 was optimal for fluorescence proteins. Additionally, aminoalcohol #10 has a strong buffering ability around pH 10 as shown in Figure S1B. Therefore, pHs in the medium could be kept between 10 to 11 through the CUBIC clearing protocol due to the daily exchange of the clearing medium. Actually, we showed the final pH values of the mixtures of erythrocyte and #10/CUBIC-1 were maintained over 10 as shown in the revised Figure 1E. Thus, we focused on the pH range between 9 to 13 in the experiment. In non-buffered basic solution, heme was efficiently released from hemoglobin, but only at pH > 11. On the other hand, aminoalcohol #10 efficiently eluted heme even in moderately basic conditions around pH 10. CUBIC-1 reagent further promoted heme release even around pH 9, which might be attributed to a combinatorial effect with urea and/or Triton X-100. These results suggested that aminoalcohol #10 in CUBIC-1 reagent expanded the pH window for efficient heme release.

To clarify the chemical properties of aminoalcohol #10 associated with its decolorizing capability, we investigated erythrocyte with a series of aminoalcohol derivatives (Figure S1E), which include primary amine (#8, #15, and Tris), secondary amine (#4), tertiary amine (#9, #10, #16, and #17) (Susaki et al., 2014) and amine bearing carboxylic acid groups (DHEG and EDTA) (Figure S1D). In the blood-decoloring by a series of aminoalcohol-related chemicals shown in Figure S1D, the mixtures were prepared according to the experiment of Figure 1E. Initial pH value in each chemical was pre-adjusted so that final pH ranges from 10.8 to 11.2. The decolorizing efficiency of primary amines is lower than those of secondary and tertiary amines (See also Figure 1F). Carboxylic groups also suppressed the decolorizing capability. These results revealed the chemical properties (i.e., higher amines without carboxylic groups) associated with efficient decolorizing and might reflect the affinity of these chemicals to the heme chromophore.

The reddish color of tissue originates mainly from the coordination of oxygen and histidine with heme in hemoglobin. Q bands (around 500–700 nm) of heme in erythrocytes treated with aminoalcohol #10 or CUBIC-1 reagent were considerably changed from those of hemoglobin-bound form (Figure 1C). Those were also different from Q bands of alkaline-denatured free form of heme. These results imply that the aminoalcohols could be tightly bound to heme porphyrin instead of oxygen and histidine in hemoglobin, which may facilitate heme release and explain the unexpected expansion of the effective pH window for heme release. We also found that secondary and tertiary amines with higher coordination capability than primary amines significantly decolorized the blood whereas related amines with a (charged) carboxyl group (DHEG and EDTA) exhibited less decolorizing capability (Figure S1D). We also note that the protonated (and hence charged) form of the aminoalcohol #10 (below its buffering pH ~10) decreased its decolorizing capability (Figure 1F). Since a heme molecule possesses an electron-deficient iron center and two negatively charged carboxyl groups, we speculated that uncharged aminoalcohol #10, which possesses highly coordinating tertiary amino groups, might have suitable chemical properties to efficiently coordinate to heme for blood decolorization.

In addition to this chemical property, the buffering capability of aminoalcohol #10 in moderately basic conditions should also contribute to the decolorizing performance. For example, hemoglobin has been usually quantified in basic Triton X-100 (pH > 13) because Triton X-100 could bind to heme in highly alkaline conditions (Wolf et al., 1984). However, the decolorization by basic Triton X-100 without buffering capability was not effective due to its variable pH (Figure 1E). Therefore, the buffering capability of aminoalcohol #10 will assist the release of heme either by Triton X-100 or aminoalcohol #10 itself. If aminoalcohol #10 did not have a buffering capability, the stable decolorizing capability may not be exerted (Figure 1F), as shown for Triton X-100 (Figure 1E). Importantly, the buffering capability of aminoalcohol #10 is exerted in moderately basic conditions, which is the optimal pH range for the fluorescence signal from GFP-related fluorescence proteins (Haupts et al., 1998). In fact, treatment of individual organs by CUBIC reagents led to much higher transmittance in the visible region than that of organs treated by other reagents (Figure S2B) while CUBIC reagents could preserve the fluorescence signal from various kinds of GFP-related fluorescence proteins (Figure S6). Taken together, two chemical properties (a heme-coordinating capability and a buffering capability in moderately basic conditions) contribute to decolorize the tissue and simultaneously preserve fluorescence signal from GFP-related fluorescence proteins.

## Mice

The  $\beta$ -actin-*mKate2* knock-in mouse ( $\beta$ -actin-nuc-3  $\times$  *mKate2*) strain was established in our laboratory. A back-bone vector for targeting, pTVCI3, harboring all of the required elements, including the thymidine kinase (TK) promoter-driven cDNA encoding Diphtheria Toxin A-fragment (DT-A) from *ROSA26* targeting vector (Abe et al., 2011) and a synthetic sequence (5'-GCGGCCGAGTACGCTAGGGATAACAGGGTAATATAGGATCCCATTTTCATTACCTCTTTCTCCGCACCCGACATAGATGATCCGTAACATAACGGTCTTAAGGTAGCGAAGATCTGGCAAACAGCTATTATGGGTATTATGGGTGATCGAAAGAACCAGCTGGGGCTCGATCCCTCGAGATCGGATATC-3') as a multiple cloning region, was constructed by inserting these sequences at the *EcoRV* site of self-concatenated pGEM-T-Easy (Promega) after removal of potential cutting sites for *PI-PspI* and *PI-SceI* from pGEM-T-Easy. The multiple cloning region of resulting pTVCI3 contains *I-SceI*, *PI-SceI*, *I-CeuI*, *PI-PspI*, *XhoI* and *EcoRV* site as single restriction site, respectively. The 3' homologous arm of  $\beta$ -actin was amplified from C57BL/6 mouse genomic DNA using PCR with the following primers: forward primer: (5'-CAGCTTGTGGCTCTGTGGCTTTGC-3', Hokkaido System Science), reverse primer: (5'-ATGAAGAGATTGCTCAGTAGTTGAGA GAGTG-3'). PCR product was treated with Mighty Cloning kit (TaKaRa) for 5'-end phosphorylation, and cloned into the *EcoRV* site of pTVCI3, and the resulting vector was designated as pTVCI3-3arm. The 5' homologous arm of  $\beta$ -actin was amplified

from C57BL/6 mouse genomic DNA using PCR with the following primers: forward primer: (5'-AACACCTCCAGTTATTGGACC ACTGG-3'), reverse primer: (5'-GTGCACTTTTATTGGTCTCAAGTCAGTG-3'). PCR product was treated with Mighty Cloning kit for 5'-end phosphorylation. pTVCI3-3arm was digested with *I*-SceI (New England BioLabs), and blunted with T4 DNA polymerase (TaKaRa). The 5' homologous arm fragment was ligated at the blunted *I*-SceI site of pTVCI3-3arm, and designated as pTVCI3-5arm-3arm. pTVCI3-5arm-3arm was digested with *PI*-SceI (New England BioLabs), blunted with T4 DNA polymerase. The Reading Frame Cassette B fragment from the Gateway Vector Conversion System (Life Technologies) was cloned into the blunted *PI*-SceI site of pTVCI3-5arm-3arm, and the resulting vector was designated as pTVCI3- $\beta$ -actin-GW. pTVCI3- $\beta$ -actin-GW was mixed with pENTR-1A\_CAG-nuc-3 × mKate2-WPRE-PuroR (Susaki et al., 2014) to perform the LR recombination reaction using the Gateway LR Clonase II Enzyme mix (Life Technologies). In the resulting targeting vector, the insertion cassette was in the same orientation as the  $\beta$ -actin gene.

C-terminal-truncated (+63) TALENs (Miller et al., 2011) that bind target sequence (5'-GGCCTGTACTGACTTGAGACCAA TAAAAGTGCACACCTTACCCTTACAC-3', TALEN binding sequences are indicated with italics) containing a polyadenylation signal sequence were designed using TALE-NT (Doyle et al., 2012). The targeting vector and TALEN-expression vector were purified and introduced into HK3i C57BL/6 mouse embryonic stem (ES) cells (Kiyonari et al., 2010) using Xfect Transfection Reagent (Clontech Laboratories, Inc. A Takara Bio Company) according to the manufacturer's instructions, and the homologous recombined, puromycin-resistant ES cell clones were isolated for further culture and expansion. An aliquot of the cells was lysed and screened for successful homologous recombination by PCR. The integrity of the targeted region was confirmed by PCR using primers annealing outside the homologous recombination arms and within the inserted cassette. The primers used for the screening and the confirmation of genome integrity were as follows: 1) forward primer annealing to the region upstream of the 5' homologous arm: 5'-CTGGCAGT CACCCAGAGACTAGC-3', 2) reverse primer annealing to the region downstream of the 5' homologous arm: 5'-GTTAGTGCA GGCCAACTTGGCCTAGG-3', 3) forward primer annealing to the region upstream of the 3' homologous arm: 5'-AGGATGG TCGCGTCCATGCCCTGAG-3', 4) reverse primer annealing to the region downstream of the 3' homologous arm: 5'-ACTTCCAGGA GCCCTATGTGGTAGC-3', 5) reverse primer annealing to the region between 5' homologous arm and Gateway cassette of pTVCI3: 5'-GGTAATGAAATGGGATCCTATATTACCC-3', and 6) forward primer annealing to the region between 3' homologous arm and Gateway cassette of pTVCI3: 5'-GAAAGAACCAGCTGGGGCTCGATCC-3'. The copy number of the inserted cassette was confirmed with a quantitative PCR assay using primers annealing to the coding sequences of the puromycin-resistance gene (forward primer: 5'-CTCGACATCGGCAAGGTGTG-3', reverse primer: 5'-GGCCTTCCATCTGTTGCTGC-3') (Susaki et al., 2014), normalized to the amount of TATA-box binding protein gene amplification (forward primer: 5'-CCCCCTCTGCACTGAAATCA-3', reverse primer: 5'-GTAGCAGCACAGAGCAAGCAA-3') (Tsuji et al., 2013) using the SYBR Premix Ex Taq GC (TaKaRa) and the ABI PRISM 7900 (Applied Biosystems). The selected ES cell clones were injected into 8-cell-stage ICR embryos to generate ~100% ES cell-derived chimeras (Kiyonari et al., 2010).

We also used the R26-H2B-EGFP (CDB0238K) mouse strain (Abe et al., 2011), the Thy1-YFP-H transgenic mouse strain (Feng et al., 2000), the R26-pCAG-nuc-3 × mKate2 mouse strain (Susaki et al., 2014), and the C57BL/6-Tg (CAG-EGFP) mouse strain (Okabe et al., 1997) to observe static fluorescent gene-expression patterns in whole-organ imaging. Mouse strains were maintained in the C57BL/6 background. We purchased the BALB/cAJcl-*nu/nu* mouse strain from CLEA Japan, Inc. and the C57BL/6-Tg (CAG-EGFP) mouse strain from Japan SLC, Inc.

All experimental procedures and housing conditions were approved by the Animal Care and the Use Committee of Graduate School of Medicine, the University of Tokyo or by the Animal Care and Use Committee of the RIKEN Kobe Institute and all of the animals were cared for and treated humanely in accordance with the Institutional Guidelines for Experiments using animals. We fed DietGel Recovery (LSG Corporation, 72-06-5022, Japan) to mice for imaging the intestine.

### Mouse Model of Streptozotocin (STZ)-Induced Diabetes

Diabetes was induced in male C57BL/6N mice at 8 weeks by a single intraperitoneal administration of saline (Otsuka Pharmaceutical Co., Ltd., 14987035081514, Japan) or 10 mg/ml streptozotocin (total 200 mg/kg, Wako Pure Chemical Industries, Ltd., 197-15153, Japan) dissolved in saline at day 0. At day 0 and day 4, blood glucose values were measured by a blood glucose monitor (GLUCOCARD G Black; ARKRAY, Inc., Japan) after fasting for 6 hr. Body weight was also measured at the same days. After four days, blood sugar levels of 36% of the mice were elevated over 300 mg/dl, which is a commonly-used criterion for the diagnosis of diabetes (Table S1). Mice with blood glucose levels over 300 mg/dl ( $n = 5$ ) at day 4 and saline-administered mice ( $n = 4$ ) were used for clearing with CUBIC (CB)-perfusion and PI staining. Imaging was performed using mice with the highest blood glucose levels of STZ group ( $n = 3$ ) and corresponding number of control group ( $n = 3$ ).

### Comparison of Clearing Methods

A number of tissue-clearing methods (including BABB, THF-DBE, Scale, SeeDB, *Clear*<sup>T</sup>, 3DISCO, CLARITY, CUBIC, and PACT-PARS) have been intensively developed. Because a simple and versatile protocol will facilitate a high-throughput approach to understanding cellular circuits in organisms, we mainly focused on the development of an immersion-only tissue-clearing protocol. Organic solvent-based clearing media such as BABB, THF-DBE decrease signals from fluorescent proteins with short duration (Ertürk et al., 2012; Hama et al., 2011). In addition, benzylalcohol and THF inherently generates potentially explosive peroxide and this also quenches the fluorescence signals of fluorescent proteins (Alnuami et al., 2008). Therefore, peroxides in benzylalcohol and THF

have to be removed by specific apparatus before use. Although organic solvent based clearing medium remains to be attractive in the clearing performance, these experimental drawbacks compelled us to focus on water-based clearing reagents. For [Figure 2A](#), we compared four chemical-based clearing methods. For collecting organ samples, adult mice (C57BL/6N and BALBc-*nu/nu*) were sacrificed by an overdose of pentobarbital (>100 mg/kg, Kyoritsu Seiyaku, Japan) and then perfused with 10 ml of 10 U/ml of heparin (Wako Pure Chemical Industries, 081-00136) in PBS (pH 7.4) and 20 ml of 4% (w/v) paraformaldehyde (PFA, Nacalai Tesque, 02890-45) in PBS via left ventricle of the heart. The excised organs (brain, heart, lung, right lobe of the liver, both side of the kidneys, pancreas, spleen, stomach, intestine, triceps surae muscle and skin) were post-fixed in 4% (w/v) PFA for 24 hr at 4°C. The specimens were washed with PBS for 20 min x three times to remove PFA just before clearing. Uncleared organs (negative control) were stocked in PBS with 0.01% Sodium Azide (Nacalai Tesque, 31208-82) at 4°C after fixation. In SeeDB standard protocol ([Ke et al., 2013](#)), the fixed organs were serially rotated (4 rpm) in 30 ml of 20%, 40%, 60% (w/v) fructose (Nacalai Tesque, 16315-55) for 8 hr each and in 30 ml of 80%, 100% (w/v) fructose for 12 hr each. From day 3, these organs were rotated in 30 ml of SeeDB (80.2% w/w fructose) at 25°C. SeeDB solution was replaced to the fresh one every day until observation. All fructose solutions contained 0.5%  $\alpha$ -thioglycerol (Tokyo Chemical Industry, S0374). In ScaleA2 and ScaleB4 protocol ([Hama et al., 2011](#)), the fixed organs were immersed in 20% (w/v) sucrose (Nacalai Tesque Inc., 30403-55, Japan) at 4°C for 24 hr. These organs were embedded in OCT compound (Sakura Finetek Japan Co., Ltd., 4583) and frozen at -80°C. The next day, they were thawed in PBS and fixed again in 4% PFA. From day 3, these organs were rotated in 30 ml of ScaleA2 (4 M urea, Nacalai Tesque, 35904-45, 10% (w/v) glycerol, Nacalai Tesque, 17018-25, and 0.1% (v/v) Triton X-100, Nacalai Tesque, 25987-85) for 2 days, 30 ml of ScaleB4 (8 M urea, 0.1% (v/v) Triton X-100) for 2 days, and 30 ml of ScaleA2 for 3 days in this order. All of the Scale solutions were replaced to the fresh one every day until observation. Two CUBIC reagents were prepared as previously reported ([Susaki et al., 2014](#)). Aminoalcohol #10 [*N,N,N',N'*-tetrakis(2-hydroxypropyl) ethylenediamine (Tokyo Chemical Industry, T0781)] is a constituent of previously published CUBIC-1 chemical cocktail. Aminoalcohol #16 [2,2',2''-nitrotriethanol (Wako Pure Chemical Industries, 145-05605)] is a constituent of previously published CUBIC-2 chemical cocktail. In brief, ScaleCUBIC-1 (CUBIC-1 reagent) was prepared as a mixture of 25 wt% urea, 25 wt% aminoalcohol #10, and 15 wt% Triton X-100. ScaleCUBIC-2 (CUBIC-2 reagent) was prepared as a mixture of 50 wt% sucrose, 25 wt% urea, 10 wt% aminoalcohol #16, and 0.1% (v/v) Triton X-100. We adopted two CUBIC protocols for this comparing experiment. For preparation of CUBIC-treated (non-perfused) samples, the fixed organs (from C57BL/6N) and skin (BALBc-*nu/nu*, to save plucking hairs before clearing) were immersed in 30 ml of CUBIC-1 reagent at 37°C with gentle shaking for 5 days. These organs were then washed with PBS and immersed in 50% glycerol at room temperature on day 6. They were immersed in 30 ml of CUBIC-2 reagent at room temperature on day 7 and at 37°C after day 8. In all four clearing methods, stomach and intestine were separately immersed from other organs to avoid contamination of sticky gastrointestinal contents.

To make CUBIC-1 reagent penetrate throughout the whole body, we also performed the CUBIC (CB)-Perfusion protocol as follows; the anesthetized mouse was perfused with 10 ml of 10 U/ml of heparin in PBS, 150 ml of 4% (w/v) PFA in PBS, 20 ml of PBS (to wash out PFA), and 20 ml of 50% (v/v) CUBIC-1 reagent (1: 1 mixture of water: CUBIC-1 reagent) in this order via left ventricle of the heart. The resulted organs were excised and continuously immersed in 30 ml of CUBIC-1 reagent at 37°C with gentle shaking for 5 days. These organs were washed with PBS, immersed in 50% glycerol in PBS at room temperature on day 5. Then, they were immersed in 30 ml of CUBIC-2 reagent at room temperature on day 6 and at 37°C after day 7. Bright-field images of adult mice (19-week-old) demonstrated that CB-Perfusion protocol markedly transparentized and decolorized adult mice ([Figures 2B](#) and [S2C](#)). Since the abdominal organs of adult mouse (including liver, pancreas, spleen, stomach, and small and large intestines) were sufficiently transparentized and decolorized, the backbones (the lumbar and sacrum vertebrae) and pelvis were easily visualized even in the ventral-to-dorsal (V-D) image of adult mice ([Figure 2B](#)). Similarly, the chest organs of adult mouse (including lung, heart, aorta, pulmonary artery and bronchi) were also highly transparentized and decolorized. Hence, the backbones (the cervical and thoracic vertebrae) and entire rib cages were easily visualized even in the ventral-to-dorsal (V-D) image of adult mice ([Figure 2B](#)). Furthermore, the muscles of limbs in adult mouse were markedly transparentized and decolorized. Therefore, the bones of forelimbs (including scapula, humerus, radius and ulna) and hindlimbs (including femur, tibia and fibula), and caudal vertebrae were clearly visualized in either V-D or the dorsal-to-ventral (D-V) images of adult mice ([Figures 2B](#) and [S2C](#)).

### Measurement of Light Transmittance

For [Figures S2A](#) and [S2B](#), we measured light transmittance of the brain, heart, lung, liver and kidney samples use in [Figure 2A](#), from 380 to 780 nm at 5 nm intervals with an integrating sphere (Spectral Haze Meter SH 7000, Nippon Denshoku Industries). We put every sample in the center of the optical cell (Nippon Denshoku Industries, 2277) without liquid to avoid sample floating. Finally, the height of the sample and the aperture of integrating sphere were adjusted before measurement.

In the instrument, two values can be determined: (1) diffused (scattered) light transmittance (%) which is the value for the light transmitted through the tissue, (2) parallel (non-diffused) light transmittance (%) which is the value for the light detected without any prevention. Diffused light transmittance was calculated as the value of (total light transmittance - parallel light transmittance) in the integrating sphere. We also calculated (100 - parallel light transmittance) as a tissue size-related value, because the sample makes a 'shadow' over the parallel light detector and the 'shadow' size is related to the sample size. Thus, the final transmittance was calculated by the diffused light transmittance divided by the value of (100 - parallel light transmittance) to be compensated with the tissue size and compared directly even between the values from different tissues. Finally, the final transmittance from four samples was averaged.

### The CUBIC Protocol for Whole-Body and -Organ Imaging

For whole body and organ imaging, we slightly modified the above CUBIC protocol to improve the transparency and quality of imaging data (Figures 2B, 3, and 4).

For whole body imaging, adult (6–19 weeks old) mouse were subjected to the same CB-Perfusion protocol as above, and then the CB-perfused mouse was immersed in 200 ml of CUBIC-1 reagent at 37°C with gentle shaking for at least two weeks. To facilitate the whole-body clearing, the reagent was refreshed daily for two weeks. The clearing medium gradually became less colored, and after two weeks the apparent transparency of the whole body became saturated. Whole-body samples can be then stored in CUBIC-1 reagent, and even shaken in 37°C over months until observation because the high pH of CUBIC-1 reagents prevents proliferation of microorganisms. The resulted sample was used for imaging and thus we did not perform further clearing with CUBIC-2 reagent.

For whole organ imaging, adult mice were subjected to the CB-Perfusion protocol as above. Organs were excised and continuously immersed in 30 ml (stomach, intestine) or 60 ml (brain, heart, lung, liver, kidneys, pancreas, spleen, muscle) of CUBIC-1 reagent at 37°C with gentle shaking at least for 7 days. To facilitate the clearing, the reagent was refreshed daily for one week, and the transparency was saturated within 10 days as in Figure 2 and S2. The samples can be then stored in CUBIC-1 reagent, and even shaken in 37°C over weeks to months to prevent proliferation of microorganisms as above. These organs were washed with PBS, immersed in 50% glycerol in PBS at room temperature, and then they were immersed in 30 ml of CUBIC-2 reagent for each group at room temperature on the first day and at 37°C after the second day. Images were acquired after 3 days incubation in CUBIC-2 reagent. For skin imaging in Figure 4E, a CAG-EGFP Tg mouse (10-week-old) was also subjected to CB-Perfusion as above. The excised skin and ear were needed to remove subcutaneous tissues and hairs, and thus we washed the specimens with PBS several times and then post-fixed and cleared according to non-perfusion protocol as above 10-day protocol. Images were acquired on day 12.

The 3D reconstitution image of heart from SYTO 16-stained nuc-3 × mKate2 demonstrated that SYTO 16 signals highlighted epicardium, papillary muscle, and right atrium whereas mKate2 signal was higher in coronary vessels (Figure 4A). The expression level of mKate2 is dependent on the cell type in each tissue because mKate2 is expressed under the control of CAG promoter in ROSA26 locus, and therefore distribution of the mKate2 fluorescent signals reflected the expression of the knocked-in expression cassette. On the other hand, SYTO 16 indiscriminately stained all cell nuclei in the tissue. Thus, distribution of the SYTO 16 fluorescent signals was attributed to the cell density in each tissue. The spatial distribution of fluorescence proteins (EGFP in Figure S6A and nuc-3 × mKate2 in Figures 4 and S5) was also markedly different. This is because EGFP was localized in the nucleus and cytosol whereas mKate2 was localized only in the nucleus. Therefore, EGFP signals were useful for the visualization of the orientation of muscular fibers in heart and muscle, whereas mKate2 signals could highlight the vascular and duct structures in heart, kidney, pancreas, and spleen. In addition, expression levels of these fluorescence proteins varied in each organ. For example, EGFP signals were more intense in the heart and the pancreas whereas mKate2 signals were elevated in the brain, the kidney, and the pancreas.

For a neonatal (postnatal day 1 or day 6) mouse clearing, 3 ml of 10 U/ml of heparin in PBS, 10 ml of 4% (w/v) PFA in PBS, 3 ml of PBS and 5 ml of 50% (v/v) CUBIC-1 reagent were perfused in this order via left ventricle of the heart after the anesthetization. Furthermore, 3 ml of CUBIC-1 reagent were additionally perfused for improving the transparency. Gastrointestinal tract was also flushed with CUBIC-1 reagent from the mouth. The mouse was then immersed in 30 ml of CUBIC-1 reagent at 37°C with gentle shaking for at least 2 weeks. To facilitate the clearing, the reagent was refreshed daily for two weeks. The samples can be then stored in CUBIC-1 reagent, and even shaken in 37°C over weeks to months to prevent proliferation of microorganisms as above. This sample was used for imaging and thus we did not perform further clearing with CUBIC-2 reagent. In the whole body imaging of P1 mouse, we noted that PI fluorescence signal was enhanced where it binds not only with DNA in the nucleus of internal organs and soft tissues but also in bone tissues (Figure 3A). Although light-sheet illumination was shaded to some extent by bone-rich structures such as paws, fluorescence signal from shaded regions was still detectable. According to the whole-body images, organ transparency was not diminished through the whole-body clearing procedure compared to clearing of individual organs separately.

Whole body and organs were stained with nucleic acid stain (propidium iodide (PI), life technologies, P21493 or SYTO 16, Life Technologies, S7578), added in 50% (v/v) CUBIC-1 reagent (for CB-Perfusion), CUBIC-1 and -2 reagents (during clearing) at a concentration of 10 µg/ml PI or 0.5 µM SYTO16, when indicated. Note that 50% (w/v) Glycerol in PBS used before CUBIC-2 reagent can be exchanged with 20% (w/v) sucrose in PBS in the original brain clearing protocol (Susaki et al., 2014).

### Microscopy

Whole-body and organ fluorescence images were acquired with light-sheet fluorescence microscopy (LSFM) (Ultramicroscope, LaVision BioTec) as reported previously (Dodt et al., 2007; Susaki et al., 2014). Samples were immersed in a 1:1 mixture of silicon oil TSF4300 (Momentive Performance Materials, RI = 1.498) and mineral oil (Sigma-Aldrich, RI = 1.467), and were put on a glass plate held with a customized sample holder. Images were captured at 0.63 × to 5 × zoom with the MVX-ZB10. Each plane was illuminated from both the right and left sides, and a merged image was saved. The exposure times were adjusted according to the fluorescent signal intensities of each sample. Detailed imaging conditions in each figure described as below; Figure 3 (A) Z-stack: 20-µm step, with 4.0 s × two illuminations for EGFP and with 0.1 s × two illuminations for PI. Zoom of the microscope: 0.63 ×, (B) Z-stack: 20-µm step, with 4.0 s × two illuminations for EGFP and with 0.1 to 0.15 s × two illuminations for PI. Zoom of the microscope: 2.0 × except 2.5 × for chest V-D images, (C) Z-stack: 20-µm step, with 0.4 to 2.0 s × two illuminations for EGFP and with 0.1 to 0.2 s × two illuminations for PI. Zoom of the microscope: 0.8 × except 1.25 × for chest V-D images, Figure 4 (A) Heart images. Z-stack: 20-µm step × 346 planes, with 0.05 s × two illuminations for SYTO 16 and with 0.5 s × two illuminations for mKate2. Zoom of

the microscope:  $2.0 \times$ . (B) Lung images. Z-stack:  $20\text{-}\mu\text{m}$  step  $\times$  306 planes, with  $0.05\text{ s}$   $\times$  two illuminations for SYTO 16 and with  $1.0\text{ s}$   $\times$  two illuminations for mKate2. Zoom of the microscope:  $1.0 \times$ . (C) Kidney images. Z-stack:  $20\text{-}\mu\text{m}$  step  $\times$  256 planes, with  $0.05\text{ s}$   $\times$  two illuminations for SYTO 16 and with  $0.5\text{ s}$   $\times$  two illuminations for mKate2. Zoom of the microscope:  $1.6 \times$ . (D) Liver images. Z-stack:  $20\text{-}\mu\text{m}$  step  $\times$  266 planes, with  $0.05\text{ s}$   $\times$  two illuminations for SYTO 16 and with  $0.5\text{ s}$   $\times$  two illuminations for mKate2. Zoom of the microscope:  $1.0 \times$ . (E) Skin and ear images. Z-stack:  $20\text{-}\mu\text{m}$  step, with  $0.2$  to  $0.5\text{ s}$   $\times$  two illuminations for EGFP and with  $0.1\text{ s}$   $\times$  two illuminations for PI. Zoom of the microscope:  $1.6 \times$  for ear,  $2.0 \times$  for skin, and  $6.3 \times$  for both magnified images, [Figure 7](#) (B) Heart images. Z-stack:  $10\text{-}\mu\text{m}$  step  $\times$  501 planes (whole image) or  $\times$  201 planes (magnified image), with  $0.1\text{ s}$   $\times$  two illuminations or  $0.1\text{ s}$   $\times$  single illumination for SYTO 16 and with  $2.0\text{ s}$   $\times$  two illuminations or  $3.0\text{ s}$   $\times$  single illumination for Cy3, respectively. Zoom of the microscope:  $2.5 \times$  or  $6.3 \times$ . (C) Lung images. Z-stack:  $10\text{-}\mu\text{m}$  step  $\times$  511 planes (whole image) or  $\times$  101 planes (magnified image), with  $0.1\text{ s}$   $\times$  two illuminations or  $0.2\text{ s}$   $\times$  two illuminations for PI and with  $2.0\text{ s}$   $\times$  two illuminations or  $3.0\text{ s}$   $\times$  two illuminations for FITC, respectively. Zoom of the microscope:  $1.6 \times$  or  $6.3 \times$ . (D) Stomach images. Z-stack:  $10\text{-}\mu\text{m}$  step  $\times$  381 planes (whole image) or  $\times$  167 planes (magnified image), with  $0.1\text{ s}$   $\times$  two illuminations or  $0.1\text{ s}$   $\times$  single illumination for SYTO 16 and with  $1.0\text{ s}$   $\times$  two illuminations or  $1.0\text{ s}$   $\times$  single illumination for Cy3, respectively. Zoom of the microscope:  $2.0 \times$  or  $6.3 \times$ . (E) Intestine images. Z-stack:  $10\text{-}\mu\text{m}$  step  $\times$  371 planes (whole image) or  $\times$  101 planes (magnified image), with  $0.1\text{ s}$   $\times$  two illuminations or  $0.1\text{ s}$   $\times$  single illumination for SYTO-16 and with  $2.0\text{ s}$   $\times$  two illuminations or  $3.0\text{ s}$   $\times$  single illumination for Cy3, respectively. Zoom of the microscope:  $1.25 \times$  or  $6.3 \times$ .

### Image Data Processing and Analysis

All raw image data were collected in a lossless 16-bit TIFF format. 3D-rendered images were visualized and captured with Imaris software (version 7.6.4 and 7.7.1, Bitplane). Brightness, contrast, and gamma of the 3D-rendered images were manually adjusted with the software at minimum when visualized.

We performed blind 3D deconvolution for a set of our LSM Z-stack images with software AutoQuant X3 (Media Cybernetics). Because the software does not have a preset for a macrozoom LSM images, we searched parameters to significantly improve the raw tiff images. Using the expert settings, we performed the 3D blind deconvolution with 50 iterations, noise manually set to 0, and the original unfiltered image as initial guess. Montage was used both in the XY and Z directions, with 15-pixel sub-volume overlap. RIs were to 1.00 and 1.49, with lens aperture at 0.15. Spacing, wavelength and magnitude settings are sample-dependent, and all other parameters were kept to the default values for the “multi-photon fluorescence” modality. Results were saved as 16-bit tiff images.

The reconstituted 3D images were then used for image analysis with Imaris software (Bitplane). In order to reliably identify all LIs in the pancreas, we acquired 6-10 sets of the magnified z-stack images to cover the entire pancreas. LIs were identified as dense clusters of PI-stained cellular nuclei in the magnified images. These images also enabled us to morphologically distinguish the characteristic clusters (LIs) from the characteristic tracts (pancreatic ducts) ([Figure 5A](#)). We identified all LIs by visual annotation of all z-stack planes in all sets of magnified images of a pancreas. The extracted LIs were then 3D-reconstituted by the surface analysis in the Imaris software. For example, yellow (in the indicated z-stack plane) and blue objects (outside the indicated z-stack plane) indicate LIs whereas green objects indicate pancreatic ducts ([Figure 5A](#)). We thus performed comprehensive and statistical analysis of diabetic LIs in the whole-pancreas of adult mice ([Figure 5B](#)). For the visualization of anatomical structures ([Figures 6, S7, and S8](#)), we selected appropriate analytical segments in each organ and manually extracted signal intensities correlated with these structures on the Surface analysis of the software. Then, each structure was manually curated and extra Surface signals were eliminated.

For extraction, counting, and volume calculation of pancreatic islets, pancreases derived from the STZ experiment and cleared by CB-Perfusion with PI staining were used. Whole-tissue 3D images of each pancreas were acquired as 6 to 10-divided region images with  $4 \times$  zoom of MVX10. The merged areas were annotated manually. Each islet was morphologically detected in the entire X-Y plane images. Then, a 3D region including one to three islets was selected for Surface analysis of Imaris software. The size of automatically selected Surface was manually adjusted to the actual islet size by changing Threshold (Absolute intensity) parameter. To remove Surfaces other than islet, Volume parameter was changed to  $10^3$  or  $10^4$  voxel number (depending on the islet size of the selected region), and manually removed the remaining Surfaces other than islet. Number and volume of islets were calculated by Imaris. Further statistical analyses between saline- or STZ- administered groups were performed using R software (Kolmogorov-Smirnov test for difference in islet size distribution, and comparison of total islets, islets larger or smaller than  $1.0 \times 10^7 \mu\text{m}^3$  for t test).

As a pilot study, we considered the automatic extraction of relevant anatomical structures in the heart and pancreas. For heart samples, analysis is performed in Fiji ([Schindelin et al., 2012](#)). We successively run the “Smooth” and “Find Edges” methods, followed by the “Tubeness” plugin (with  $\sigma = 1$ ). Finally, we apply a binary mask to keep only pixels with intensity higher than 400. As shown in [Figure S7B](#), the method successfully extracts coronary arteries and most of them were merged to the manual extracted Surface signal in Imaris. For the pancreas samples, the objective is to accelerate the identification of Langerhans islets. Our method relies on two properties of these islets: (a) even though their intensity varies, the islets are generally brighter than their immediate surroundings; (b) islets have a roughly spherical shape. The first property is used in the pre-processing method, implemented in C++. Using a sliding window, we measure the average intensity in each region of each Z-slice of the 3D image, and only keep pixels with intensity at least 10% higher than this local average. All other pixels are set to 0. Each pre-processed 2D slice is then analyzed in Fiji. We run the “Find Edges” method, followed by computing of the largest absolute eigenvalue of the Hessian matrix (using the corresponding FeatureJ plugin with smoothing = 1), to identify clusters that do not have the desired shape. At each pixel, the eigenvalue

is then multiplied by seven and subtracted from the current intensity. We save the resulting file for each slice, and re-construct the 3D image. While the method still needs to be refined, early results on the clearest slices are encouraging (Figure 5C). For darker slices, curation of the result file removes inaccurate annotations. This process will be automatized in future versions.

### 3D Immunostaining of CUBIC Samples

3D IHC protocol for CUBIC samples was according to our previous paper (Susaki et al., 2014). Organ samples with CB-Perfusion were treated with CUBIC-1 for 7 days, washed with PBS, immersed in 20% (w/v) sucrose in PBS, and frozen in O.C.T. compound at  $-80^{\circ}\text{C}$  overnight. The frozen samples were then thawed, washed with PBS, and subjected to immunostaining with the 1:100 diluted fluorescent-labeled antibodies in 5 ml of 2% (v/v) Triton X-100 in PBS for 3 days at  $4^{\circ}\text{C}$  with rotation. The stained samples were then washed with 5 ml of PBS several times at  $37^{\circ}\text{C}$  with rotation. The stained samples were then immersed in CUBIC-2 for 4 to 15 hr. The following antibodies were used for the staining: Cy3-conjugated anti- $\alpha$ -smooth muscle actin ( $\alpha$ -SMA) antibody produced in mouse (Sigma, C6198) for heart, stomach, and intestine, and monoclonal FITC-conjugated anti-Pan cytokeratin antibody [C-11] (abcam, ab78478) for lung. These antibodies were mixed with the samples after filtration with an Ultrafree-MC GV Centrifugal Filter (Millipore UFC30GV00).

### SUPPLEMENTAL REFERENCES

Doyle, E.L., Booher, N.J., Standage, D.S., Voytas, D.F., Brendel, V.P., Vandyk, J.K., and Bogdanove, A.J. (2012). TAL Effector-Nucleotide Targeter (TALE-NT) 2.0: tools for TAL effector design and target prediction. *Nucleic Acids Res.* 40 (Web Server issue), W117–W22.

Kiyonari, H., Kaneko, M., Abe, S., and Aizawa, S. (2010). Three inhibitors of FGF receptor, ERK, and GSK3 establishes germline-competent embryonic stem cells of C57BL/6N mouse strain with high efficiency and stability. *Genesis* 48, 317–327.

Miller, J.C., Tan, S., Qiao, G., Barlow, K.A., Wang, J., Xia, D.F., Meng, X., Paschon, D.E., Leung, E., Hinkley, S.J., et al. (2011). A TALE nuclease architecture for efficient genome editing. *Nat. Biotechnol.* 29, 143–148.

Tsujino, K., Narumi, R., Masumoto, K.H., Susaki, E.A., Shinohara, Y., Abe, T., Iigo, M., Wada, A., Nagano, M., Shigeyoshi, Y., and Ueda, H.R. (2013). Establishment of *TSH  $\beta$*  real-time monitoring system in mammalian photoperiodism. *Genes Cells* 18, 575–588.

Wolf, H.U., Lang, W., and Zander, R. (1984). Alkaline haematin D-575, a new tool for the determination of haemoglobin as an alternative to the cyanhaemoglobin method. II. Standardisation of the method using pure chlorohaemin. *Clin. Chim. Acta* 136, 95–104.

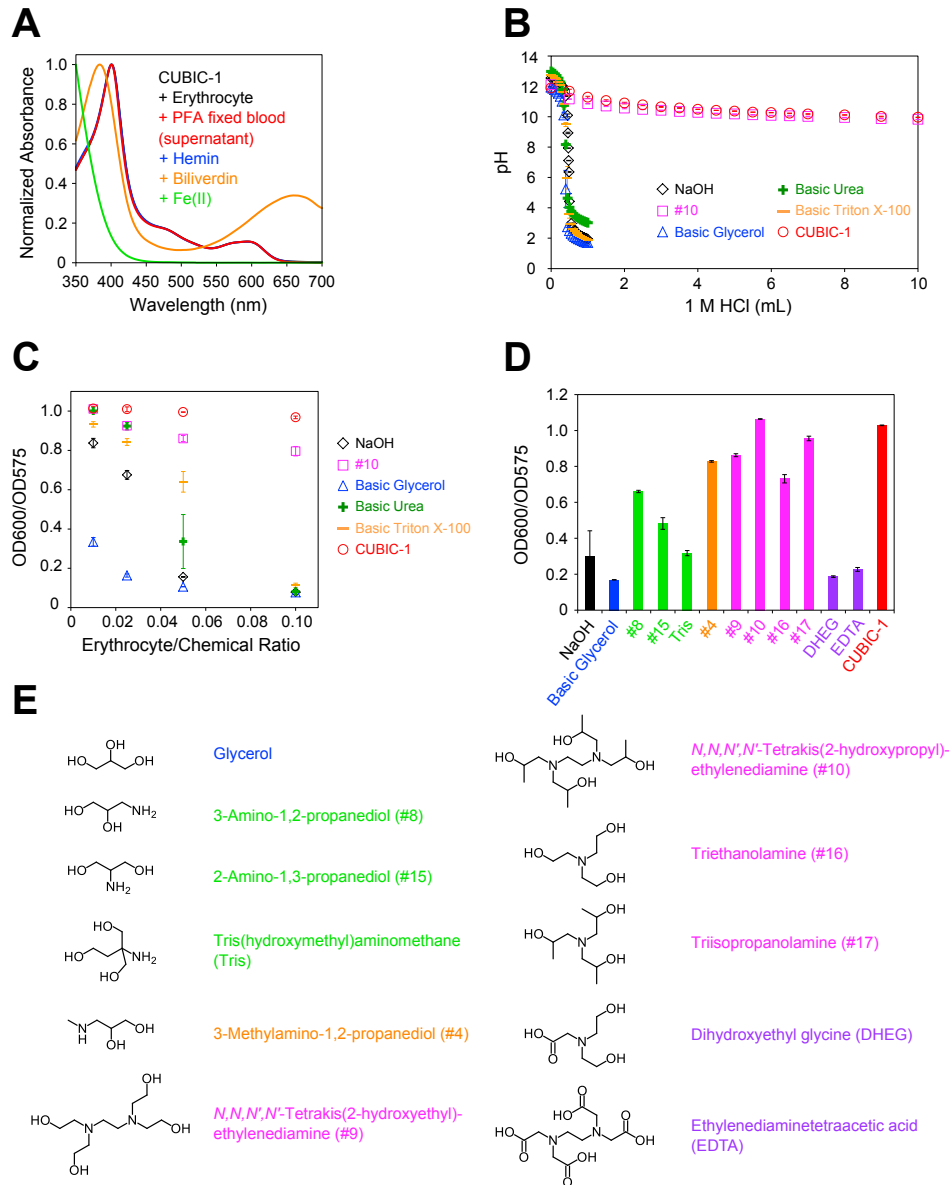


**Figure S1. Aminoalcohols in CUBIC Cocktails Decolorized the Blood by Efficiently Eluting Heme Chromophore, Related to Figure 1**

(A) Normalized visible spectra of 0.1% mouse erythrocyte (black), 1/10 diluted supernatant from Figure 1A (red), 10  $\mu$ M hemin (blue), 10  $\mu$ M biliverdin (orange), and 100  $\mu$ M iron(II) chloride (green), in CUBIC-1 reagent.

(B) 50 g of CUBIC-1 reagent (red circle,  $n = 3$ ), 25 wt% aminoalcohol #10 (magenta square,  $n = 3$ ), 25 wt% basic glycerol (blue triangle,  $n = 3$ ), 25 wt% basic urea (green cross,  $n = 3$ ), 15 wt% basic Triton X-100 (orange bar,  $n = 3$ ), or 0.01 M NaOH (black diamond,  $n = 3$ ) were titrated with 1 M HCl. pHs are plotted against the titrated volume of 1 M HCl. Data represent the average  $\pm$  SD.

(C) OD600/575 values of 1% to 20% erythrocyte solution mixed with CUBIC-1 reagent (red circle,  $n = 3$ ), 25 wt% aminoalcohol #10 (magenta square,  $n = 3$ ), 25 wt% basic glycerol (blue triangle,  $n = 3$ ), 25 wt% basic urea (green cross,  $n = 3$ ), 15 wt% basic Triton X-100 (orange bar,  $n = 3$ ), and 0.01 M NaOH (black diamond,  $n = 3$ ) in Figure 1E are plotted against erythrocyte/chemical mixture ratio. Data represent the average  $\pm$  SD.

(D) OD600/575 values of 1% erythrocyte solution mixed with a series of aminoalcohols [primary amine (green,  $n = 3$ ), secondary amine (orange,  $n = 3$ ), tertiary amine (magenta,  $n = 3$ ), or amine bearing carboxylic acid (purple,  $n = 3$ ), NaOH (black,  $n = 3$ ), basic glycerol (blue,  $n = 3$ ) or CUBIC-1 reagent (red,  $n = 3$ ) is shown. Initial pH value in each chemical was pre-adjusted so that final pH ranges from 10.8 to 11.2. Data represent the average  $\pm$  SD.

(E) Chemical structures of glycerol and a series of aminoalcohols examined in this study. Numbering of the chemicals was derived from the previous chemical screening. Glycerol is a polyhydric alcohol without an amine group. 3-Amino-1,2-propanediol (#8), 2-amino-1,3-propanediol (#15), and tris(hydroxymethyl)aminomethane (Tris) are aminoalcohols with primary amine. 3-Methylamino-1,2-propanediol (#4) is an aminoalcohol with a secondary amine group. *N,N,N',N'*-Tetrakis(2-hydroxyethyl)ethylenediamine (#9), *N,N,N',N'*-tetrakis(2-hydroxypropyl)ethylenediamine (#10), triethanolamine (#16), and triisopropanolamine (#17) are aminoalcohols with a tertiary amine group. Dihydroxyethyl glycine (DHEG) and ethylenediaminetetraacetic acid (EDTA) are amines with carboxylic groups.

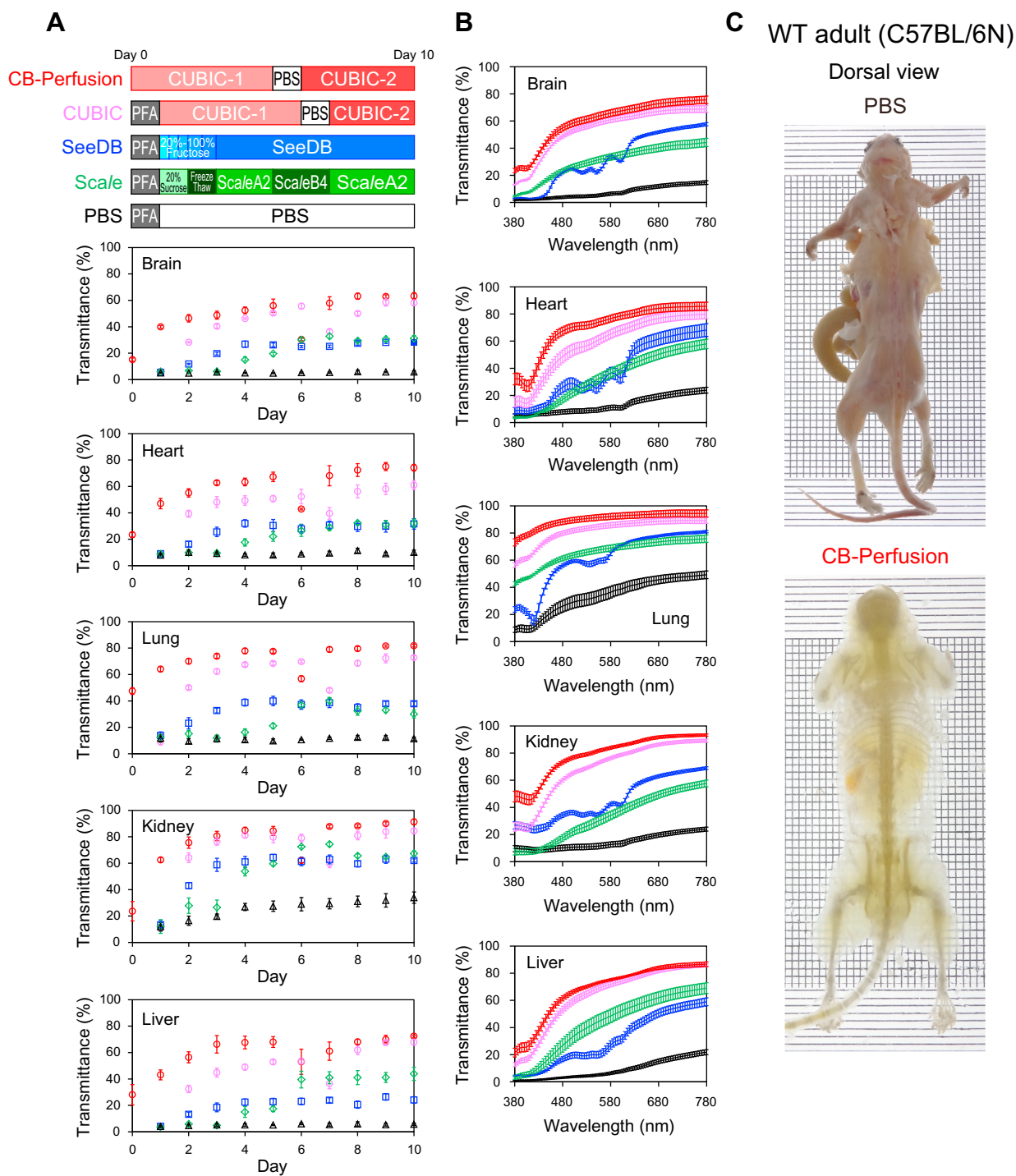


**Figure S2. CUBIC Is a Simple and Efficient Whole-Organ and Whole-Body Clearing Protocol, Related to Figure 2**

(A) Temporal development of transmittance of different organs (brain, heart, lung, kidney, and liver) with each protocol. Average light transmittance of fixed whole organs treated with PBS (black,  $n = 4$ ), the Scale protocol (green,  $n = 4$ ), the SeeDB protocol (blue,  $n = 4$ ), the CUBIC protocol (pink,  $n = 4$ ) or the CB-Perfusion protocol (red,  $n = 4$ ), were measured. Data represent the average  $\pm$  SD.

(B) Transmission curves of different organs (brain, heart, lung, kidney, and liver) with each protocol after 10 days. Light transmittance around the visible region (380–780 nm) of fixed whole organs treated with PBS (black,  $n = 4$ ), Scale protocol (green,  $n = 4$ ), SeeDB protocol (blue,  $n = 4$ ), CUBIC protocol (pink,  $n = 4$ ) or the CB-Perfusion protocol (red,  $n = 4$ ) were measured. Data represent the average  $\pm$  SD.

(C) Bright-field images (dorsal view) of fixed whole body (C57BL/6N adult mice) stocked in PBS or subjected to the CB-Perfusion protocol, also shown in Figure 2B. 8-week-old mouse for the PBS sample and 19-week-old mouse for the cleared sample are shown.

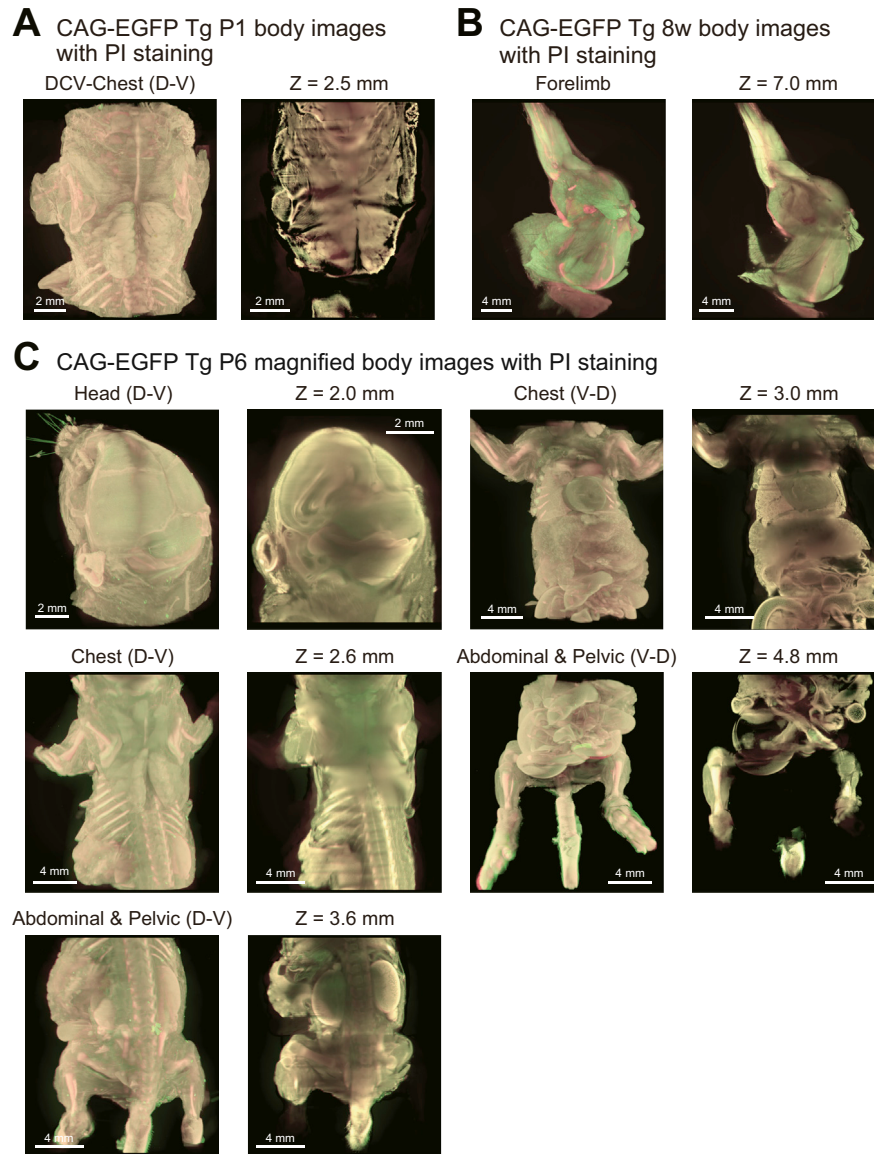


**Figure S3. CUBIC Is Applicable to Whole-Body Imaging of Infant and Adult Mice with Single-Cell Resolution, Related to Figure 3**

(A) 3D-reconstituted and X-Y plane body images of PI-stained CAG-EGFP Tg P1 mouse. Chest organs (D-V) are shown. The image was deconvolved with AutoQuant X3 software. Z-stack: 20- $\mu$ m step, with 4.0 s  $\times$  two illuminations for EGFP and with 0.1 to 0.15 s  $\times$  two illuminations for PI. Zoom of the microscope: 2.0  $\times$ . Prefix "DCV-" indicates the deconvolved image.

(B) 3D-reconstituted and X-Y plane body images of the PI-stained CAG-EGFP Tg adult mouse (8-week-old). Forelimb is shown. Z-stack: 20- $\mu$ m step, with 0.4 to 2.0 s  $\times$  two illuminations for EGFP and with 0.1 to 0.2 s  $\times$  two illuminations for PI. Zoom of the microscope: 0.8  $\times$ .

(C) 3D-reconstituted and X-Y plane (indicated with Z position) body images of the PI-stained CAG-EGFP Tg P6 mouse. Head (D-V), chest organs (V-D and D-V), abdominal and pelvic organs (V-D and D-V) are shown. Z-stack: 20- $\mu$ m step, with 4.0 s  $\times$  two illuminations for EGFP and with 0.1 s  $\times$  two illuminations for PI. Zoom of the microscope: 1.25  $\times$  except 2.0  $\times$  for head D-V image.

## CAG-EGFP Tg P1 magnified organ images with PI staining

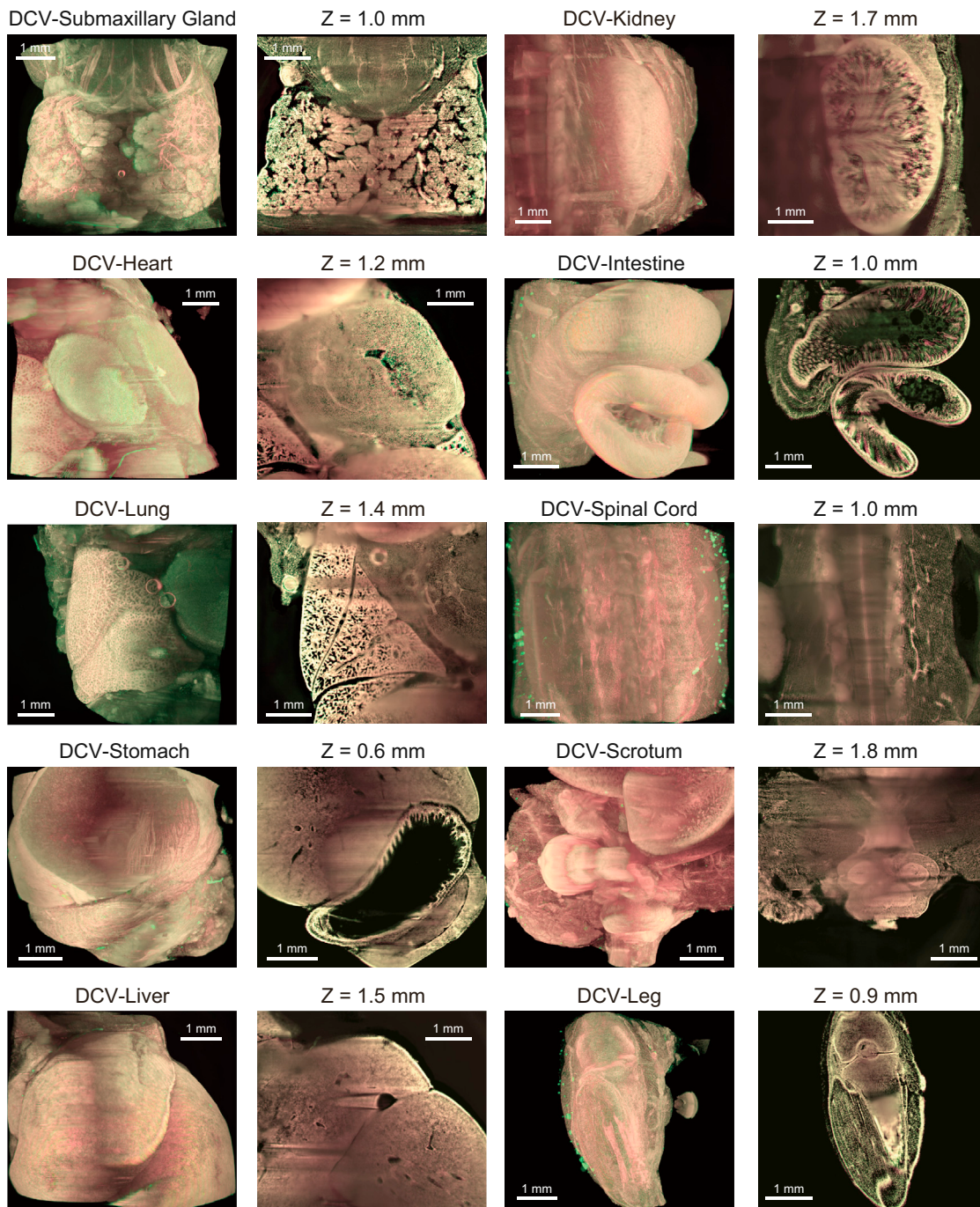


**Figure S4. Magnified Organ Images of CAG-EGFP Tg P1 Mouse, Related to Figure 3**

3D-reconstituted magnified organ images (submaxillary gland, heart, lung, stomach, liver, kidney, intestine, spinal cord, scrotum, and leg) of the PI-stained CAG-EGFP Tg P1 mouse were acquired with LSMF. All images were deconvolved with AutoQuant X3 software. Z-stack: 20- $\mu$ m step, with 4.0 s  $\times$  two illuminations for EGFP and with 0.1 to 0.2 s  $\times$  two illuminations for PI. Zoom of the microscope: 5.0  $\times$ . Note that the structures inside the spiral canal or leg bones were detected (panels of spinal cord and leg). Prefix "DCV-" indicates the deconvolved image.

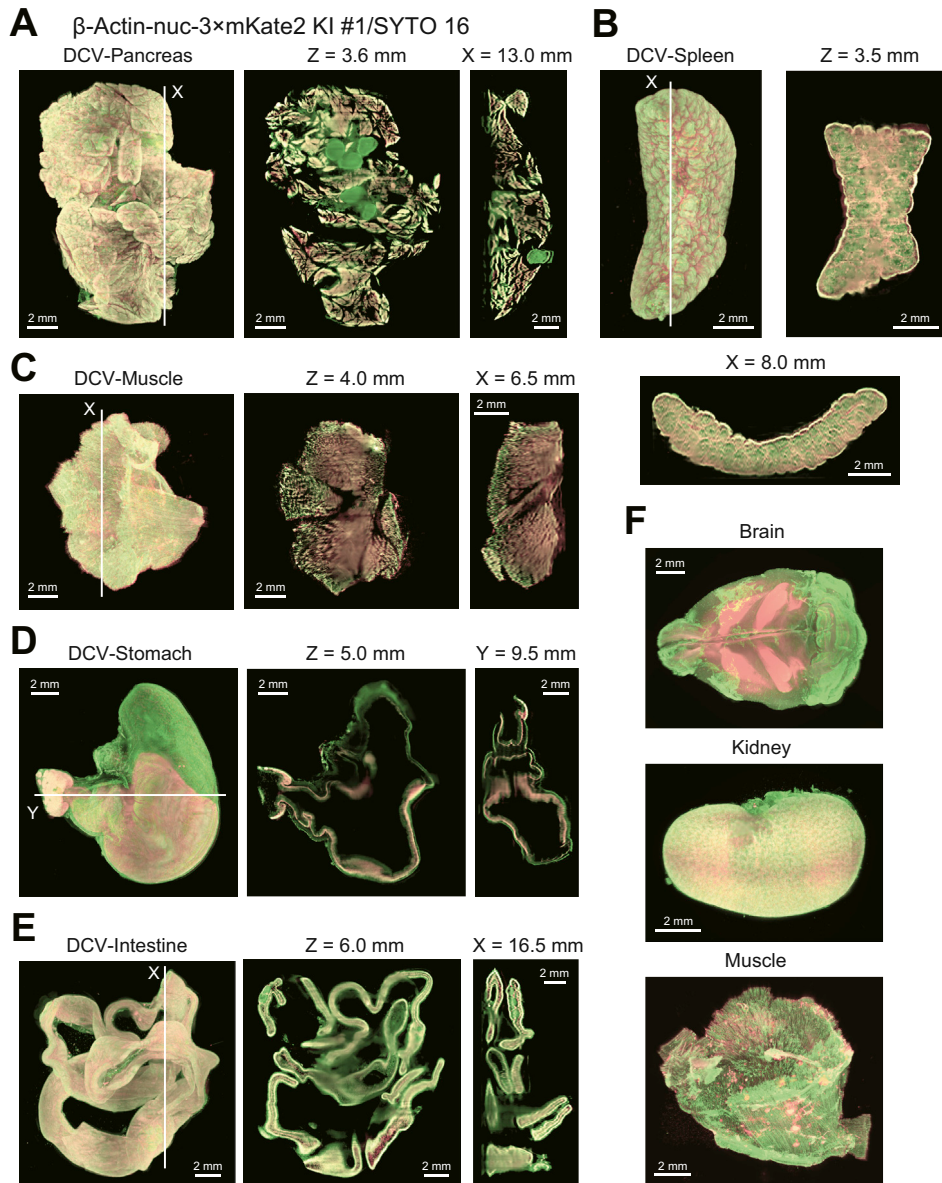


**Figure S5. CUBIC Is Applicable to Whole-Organ Imaging with Single-Cell Resolution, Related to Figure 4**

(A–F) The reconstituted 3D and section images of the SYTO 16-stained mouse pancreas (A), spleen (B), soleus muscle (C), stomach (D), intestine (E), brain, another kidney (contralateral to the kidney shown in Figure 4C), and another soleus muscle (contralateral to the soleus muscle shown in Figure S5C) (F), of  $\beta$ -actin-nuc-3  $\times$  mKate2 KI mouse (8-week-old) were acquired with LSFM. In (A–E), images were deconvolved with AutoQuant X3 software. Raw X–Y section images, and reconstituted Y–Z and X–Z section images are at the indicated positions.

(A) Pancreas images. Z-stack: 20- $\mu$ m step  $\times$  321 planes, with 0.05 s  $\times$  two illuminations for SYTO 16 and with 0.5 s  $\times$  two illuminations for mKate2. Zoom of the microscope: 1.25  $\times$ .

(B) Spleen images. Z-stack: 20- $\mu$ m step  $\times$  231 planes, with 0.05 s  $\times$  two illuminations for SYTO 16 and with 1.0 s  $\times$  two illuminations for mKate2. Zoom of the microscope: 1.6  $\times$ .

(C) Soleus muscle images. Z-stack: 20- $\mu$ m step  $\times$  331 planes, with 0.10 s  $\times$  two illuminations for SYTO 16 and with 2.0 s  $\times$  two illuminations for mKate2. Zoom of the microscope: 1.6  $\times$ .

(D) Stomach images. Z-stack: 20- $\mu$ m step  $\times$  396 planes, with 0.05 s  $\times$  two illuminations for SYTO 16 and with 1.0 s  $\times$  two illuminations for mKate2. Zoom of the microscope: 1.25  $\times$ .

(E) Intestine images. Z-stack: 20- $\mu$ m step  $\times$  366 planes, with 0.05 s  $\times$  two illuminations for SYTO 16 and with 2.0 s  $\times$  two illuminations for mKate2. Zoom of the microscope: 1.0  $\times$ .

(F) The reconstituted 3D images of brain, contralateral kidney, and contralateral muscle. Zoom of the microscope: 1.25  $\times$  for brain, 2.0  $\times$  for kidney, and 1.6  $\times$  for muscle. Prefix “DCV-” indicates the deconvolved image.

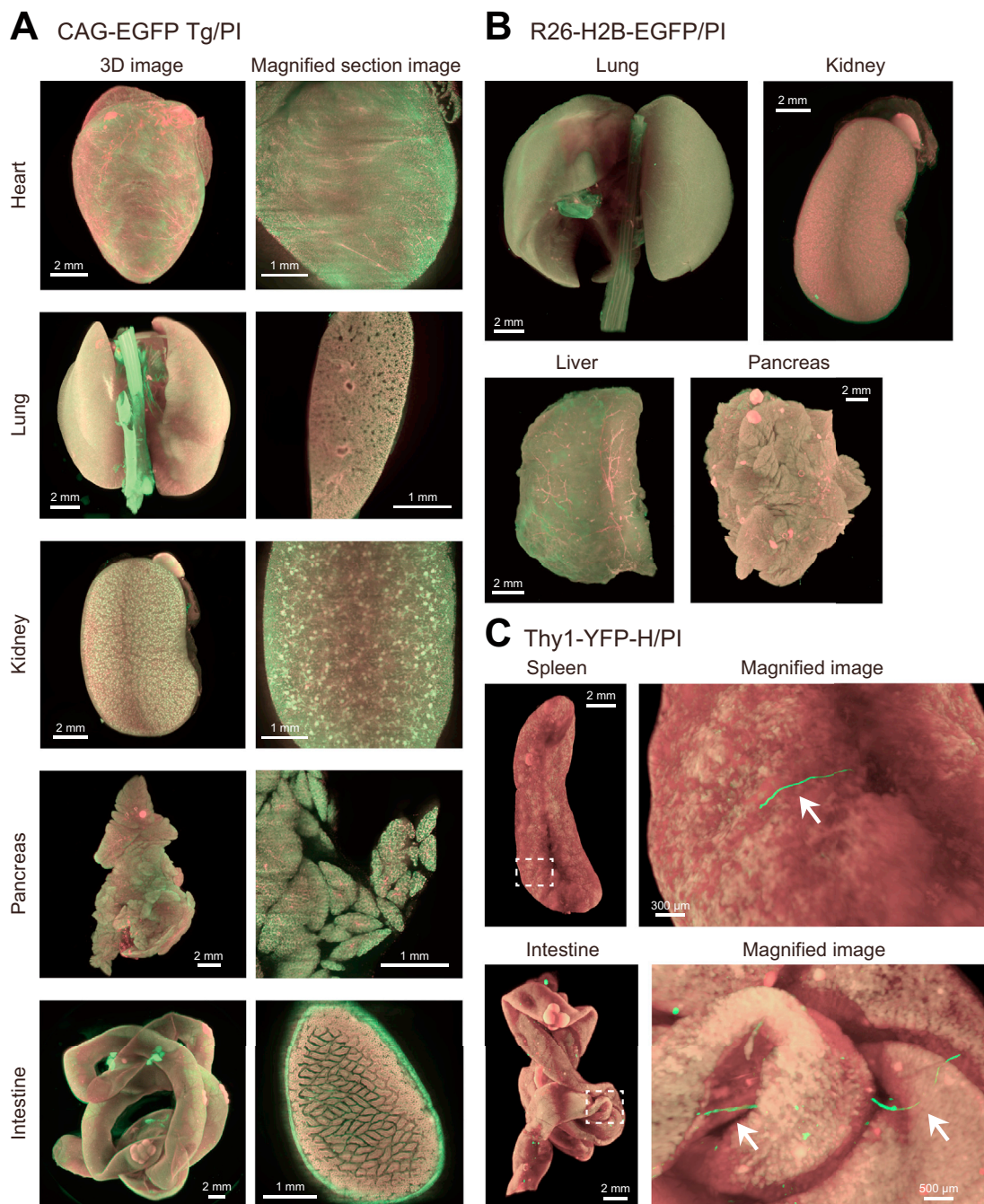


**Figure S6. CUBIC Is Applicable to the Whole-Organ Imaging of Various Fluorescent Proteins, Related to Figure 4**

(A) The reconstituted 3D whole-organ and magnified section images of heart, lung, kidney, pancreas, and intestine from CAG-EGFP Tg mouse (8-week-old) were acquired with LSFM. The magnified section images of EGFP/PI merged signals at the approximate 1 mm depth of each organ. Z-stack: 20- $\mu$ m step, with 0.3 to 2.0 s  $\times$  two illuminations for EGFP and with 0.1 to 0.4 s  $\times$  two illuminations for PI. Zoom of the microscope: 0.8  $\times$  for intestine, 1.0  $\times$  for pancreas, 1.25  $\times$  for lung, 1.6  $\times$  for heart and kidney, and 5.0  $\times$  for all magnified section images.

(B) The reconstituted 3D whole-organ images of lung, kidney, liver, and pancreas from R26-H2B-EGFP KI mouse (4-month old) were acquired with LSFM. Z-stack: 20- $\mu$ m step, with 2.0 s  $\times$  two illuminations for EGFP and with 0.1 to 0.3 s  $\times$  two illuminations for PI. Zoom of the microscope: 1.0  $\times$  for pancreas, 1.25  $\times$  for lung, liver, and kidney.

(C) The reconstituted 3D whole-organ images of spleen and intestine from Thy1-YFP-H Tg mouse (8-week-old) were acquired with LSFM. Z-stack: 20- $\mu$ m step, with 0.7 to 2.0 s  $\times$  two illuminations for YFP and with 0.1 to 0.3 s  $\times$  two illuminations for PI. Zoom of the microscope: 0.8  $\times$  for intestine and 1.25  $\times$  for spleen. Magnified 3D images are at the indicated positions. Arrow indicates neurons.

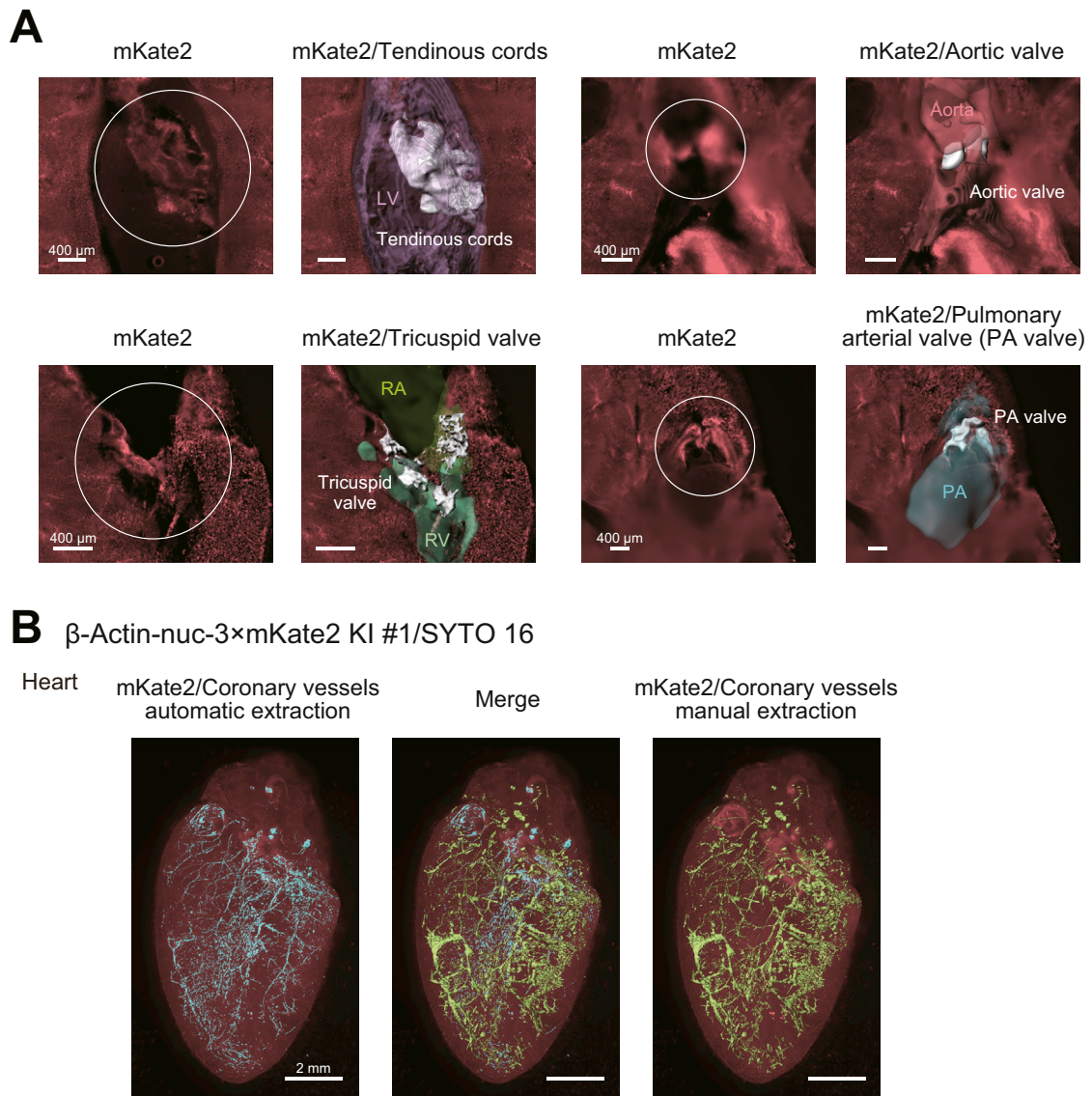


**Figure S7. CUBIC Is Applicable to the 3D Anatomy of Organs, Related to Figure 6**

Manual extraction of internal structures was performed with Surface analysis of Imaris software. The reconstituted 3D images of the heart from the SYTO 16-stained  $\beta$ -actin-nuc-3  $\times$  mKate2 KI mouse (8-week-old) in Figure 4 were used. After Surface extraction by the software, each structure was manually curated and extra Surface signals were eliminated.

(A) Detailed views of heart valves and surrounding structures. Cross sectional mKate2 images and surrounding structures (Surface volume, 3D) are shown.

(B) Automatic identification of coronary vessels. Left panel: automated extraction of coronary vessels with Fiji-based pipeline. Right panel: manual extraction of coronary vessels with Imaris in Figure 6A (view from different direction). Extracted vessels with these two methods are merged in the center panel.

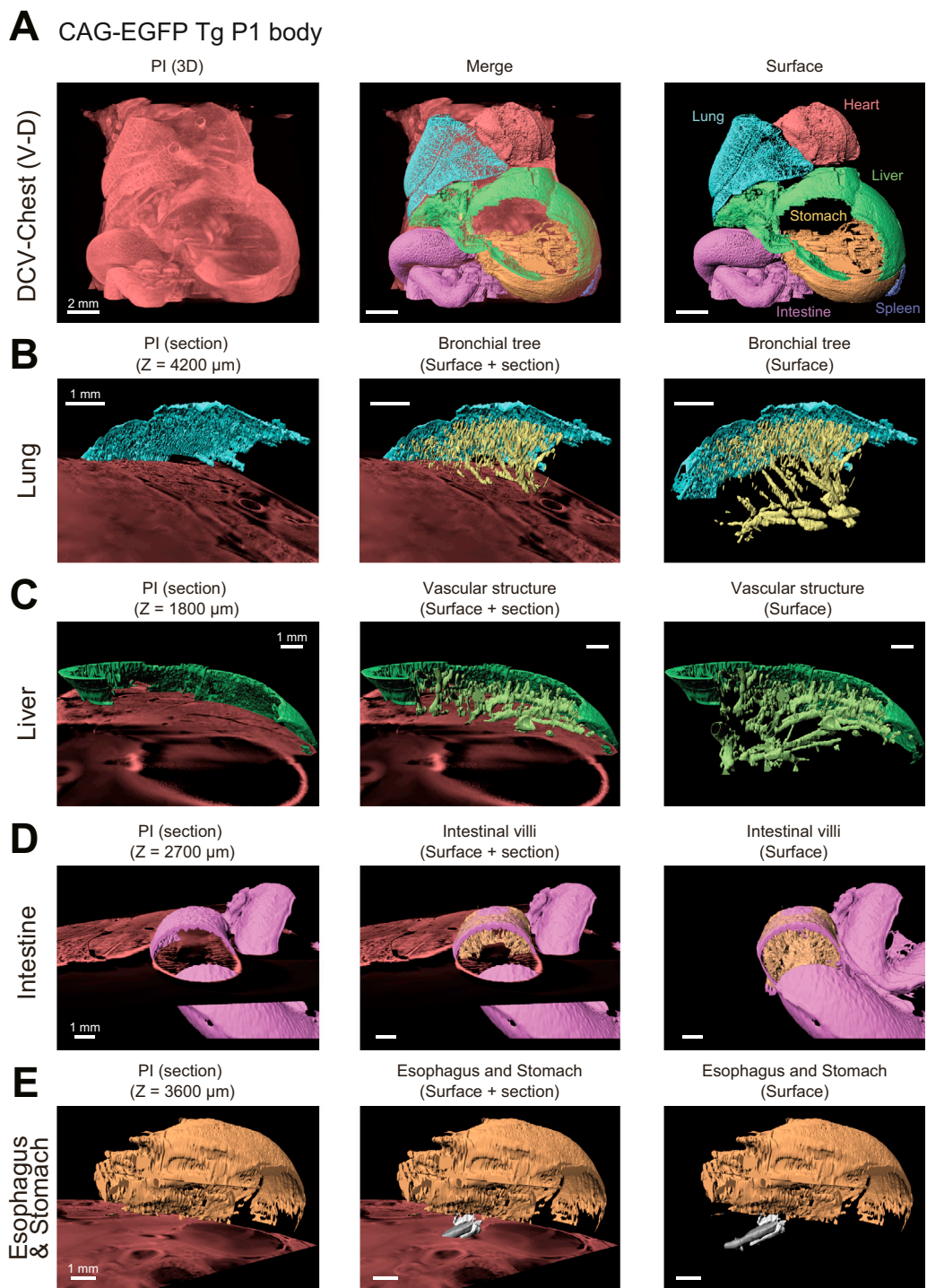


**Figure S8. CUBIC Is Applicable to the 3D Anatomy of Infant Body, Related to Figure 6**

(A–E) Extraction of internal structures was performed with surface analysis of Imaris software, similar in Figure 6. The reconstituted 3D images of the chest (A), lung (B), liver (C), intestine (D), and esophagus and stomach (E) from the PI-stained CAG-EGFP Tg P1 mouse in Figure 3B were used. After surface extraction by the software, each structure was manually curated and extra surface signals were eliminated. (A) Overview of organ identification using the chest 3D image with single-cell resolution. Prefix “DCV-” indicates the deconvolved image. (B) – (E) Extraction and visualization of the bronchial tree (yellow) with organ surface (light blue) of lung in (B), vascular structure (olive) with organ surface (green) of liver in (C), intestinal wall (purple) and villi (peachpuff) in (D) and stomach (brown), esophagus (gray) and esophageal gland (light gray) in (E).